



**HARVEST4D**

HARVESTING DYNAMIC 3D WORLDS FROM COMMODITY SENSOR CLOUDS

## Publications for Task 6.3

### Deliverable 6.31

Date: 2015-07-08  
Grant Agreement number: EU 323567  
Project acronym: HARVEST4D  
Project title: Harvesting Dynamic 3D Worlds from Commodity Sensor Clouds

## Document Information

<b>Deliverable number</b>	D6.31
<b>Deliverable name</b>	Publications for Task 6.3
<b>Version</b>	1.2
<b>Date</b>	2015-07-08
<b>WP Number</b>	6
<b>Lead Beneficiary</b>	TUD
<b>Nature</b>	R
<b>Dissemination level</b>	PU
<b>Status</b>	Final
<b>Author(s)</b>	TUD

## Revision History

Rev.	Date	Author	Org.	Description
0.1	2015-05-29	Samir Aroudj	TUD	First draft
0.2	2015-06-26	Tobias Plötz	TUD	Condensed
0.3	2015-06-29	Samir Aroudj	TUD	Checked
1.0	2015-07-08	Samir Aroudj, Tobias Plötz	TUD	Final version
1.1	2015-07-13	Michael Weinmann	UBO	Final version updated
1.2	2015-07-13	Samir Aroudj	TUD	Corrections

## Statement of originality

This deliverable, although of public dissemination level, may at the time of delivery still contain original unpublished work (e.g., accepted papers that are not public yet, or papers under revision). Acknowledgement of previously published material and of the work of others has been made through appropriate citation, quotation or both.

---

## TABLE OF CONTENTS

1	Executive Summary .....	1
1.1	Introduction .....	1
1.2	Publications .....	1
1.3	Additional References .....	1
2	Description of Publications .....	2
2.1	Overview .....	2
2.2	3D Scene Flow Estimation with a Piecewise Rigid Scene Model .....	2
2.3	Multi-View Normal Field Integration for 3D Reconstruction of Mirroring Objects .....	3
3	Appendix .....	4

---

## 1 EXECUTIVE SUMMARY

### 1.1 INTRODUCTION

The publications that resulted from task 6.3 are described in this deliverable. Furthermore, this deliverable presents how these publications fit into the project work plan.

Task 6.3 has the following objective. The work package aims to improve reconstruction of geometric models in both accuracy and completeness by means of additionally separating transient and permanent portions of captured scenes besides static Multi-View Stereo data. The research results presented here address the problem of simultaneously reconstructing 3D scene geometry together with its 3D motion.

Two publications are mainly associated with task 6.3 which are attached to the appendix of this deliverable.

### 1.2 PUBLICATIONS

The following publications can be found in the appendix:

- Christoph Vogel, Konrad Schindler and Stefan Roth  
*3D Scene Flow Estimation with a Piecewise Rigid Scene Model*  
International Conference on Computer Vision (ICCV, 2015, 1-28)
- Michael Weinmann, Aljosa Osep, Roland Ruiters, and Reinhard Klein  
*Multi-View Normal Field Integration for 3D Reconstruction of Mirroring Objects*  
International Conference on Computer Vision (ICCV), pp. 2504-2511, 2013

### 1.3 ADDITIONAL REFERENCES

The input images of the example results in the main paper are from the following source:

- Stephan Meister, Bernd Jähne, and Daniel Kondermann  
*Outdoor Stereo Camera System for the Generation of Real-world Benchmark Data Sets*  
Optical Engineering 51.2 (2012)



---

## 2 DESCRIPTION OF PUBLICATIONS

### 2.1 OVERVIEW

The publication [Vogel et al. 2015] addresses an important aspect of the Harvest4D project as the method processes input data from various sources at different time instants to compute a single, consistent, dynamic and dense representation of the scene geometry. In this approach, motion is detected and explicitly taken into account for improved dense geometry reconstruction.

The technique proposed in [Weinmann et al. 2013] achieves dense geometry reconstruction of mirroring objects in a different way by detection and exploitation of light patterns projected onto the surface of a target object.

### 2.2 3D SCENE FLOW ESTIMATION WITH A PIECEWISE RIGID SCENE MODEL

The estimation of scene flow of a dynamic 3D environment means to jointly reconstruct dense geometry and its 3D motion from images taken by two or more cameras at multiple time instants. Scene flow estimation generalizes optical flow to 3D or, alternatively, dense multi-view stereo to dynamic scenes as they are targeted by the Harvest4D project. In order to make this challenging task tractable, the publication assumes a world made up of rigidly moving planes, an assumption that is approximately correct in urban environments. The main goal is then to recover the extent and the motion of each plane.

The main contribution of the publication is a view-consistent multi-frame scheme devised together with a piecewise rigid and planar scene model. Each camera view is taken into account for model computation and is associated with its own scene representation, which consists of a set of rigidly moving 3D planes to which individual pixels are assigned. Importantly, these representations are optimized to be consistent across all viewpoints and a few frames within a short temporal window. The time-consistency is based on the assumption that 3D rigid motion is approximately constant over a short time period. The joint optimization of pixel assignments and plane parameters leverages robust discrete labeling methods and efficient proposal generation.

The proposed approach has the following advantages. Unlike classical stereo or MVS, which only considers static geometry, it also takes scene movements into account as it also includes a generalization of 2D optical flow. Moreover, the plane-based scene representation is significantly more parsimonious than previous pixel-based scene models. Additionally, the 3D flow representation allows for a better exploitation of the piecewise constant motion assumption and therefore a larger time window, since physical properties such as inertia are not invalidated by projection of scene flow to 2D. The view-consistent multi-frame scheme enables processing of many images as they can be taken from all camera views of frames near some time instant  $t$  to infer a scene model at time  $t$  in a strongly robust and highly accurate way. The scene model with its optimization approach also enables the definition of suitable scene priors, efficient and effective occlusion reasoning, outlier and missing information handling.

Concerning both flow and stereo, the method achieves leading performance on the KITTI benchmark. Figure 1 presents results of the scene flow method for input images from [Meister et al. 2012].

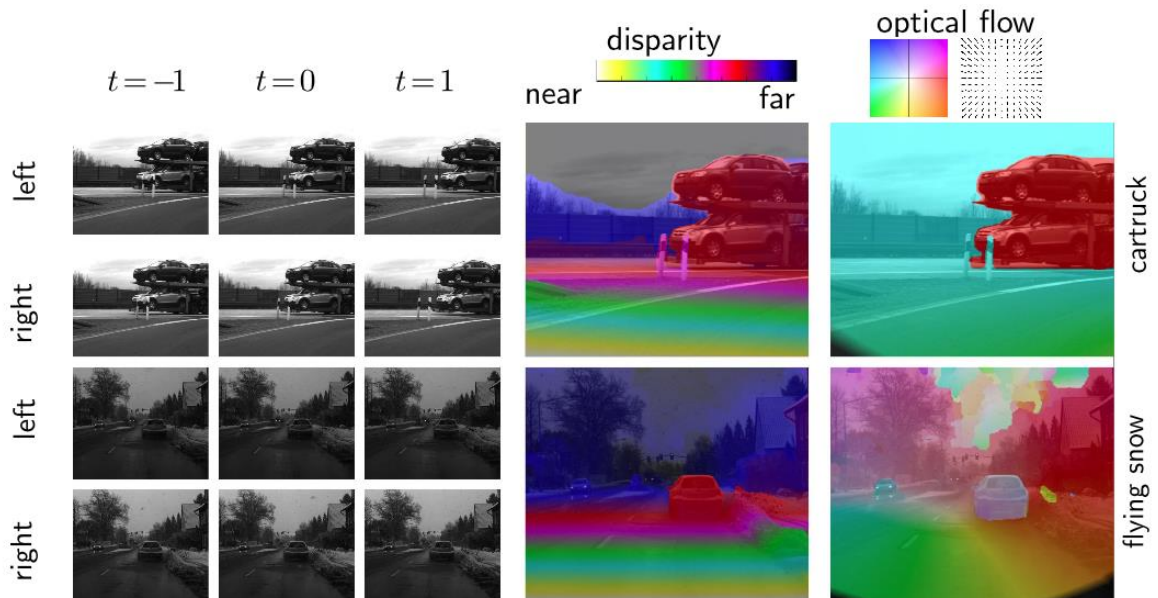


Figure 1 shows two challenging examples for scene flow estimation. Input images of a stereo setup and a three frames time window (left), scene geometry and 3D motion reprojected to disparity (center) and optical flow (right).

### 2.3 MULTI-VIEW NORMAL FIELD INTEGRATION FOR 3D RECONSTRUCTION OF MIRRORING OBJECTS

The technique proposed in [Weinmann et al. 2013] focuses on dense geometry reconstruction of mirroring objects by introducing a novel, robust, multi-view normal field integration technique. The object of interest is illuminated with a series of patterns emitted by displays. The respective information observed by a camera allows calculation of individual volumetric normal fields for each combination of camera and illumination configuration.

Depending on the local surface curvature or due to non-perfect mirroring surface characteristics, not all of the projected stripe patterns are reliably decoded. Consequently, we locally adapt the decoding to the finest still resolvable pattern resolution. The per-view normal information is projected into the volume. As occlusions, outliers from interreflections or noise likely occur for the rather complicated object geometries to be expected, the resulting normal fields typically contain regions with missing or even unreliable observations which makes a robust reconstruction complicated. However, using a non-parametric clustering of normal hypotheses derived for each point in the scene allows us to derive both the local surface normal which is most likely and a local surface consistency estimate. Based on these two estimates per point in the considered volume, a variational method is afterwards applied where an iterative min-cut approach is used to

reconstruct the surface geometry. Finally, the surface is refined by means of the measured normals.

Our technique allows high-quality reconstructions not only for synthetic data but also for real-world data. Furthermore, several parts of this framework can be used in a more general way. For example, normals derived via other principles such as photometric stereo might also serve as input for the optimization framework.

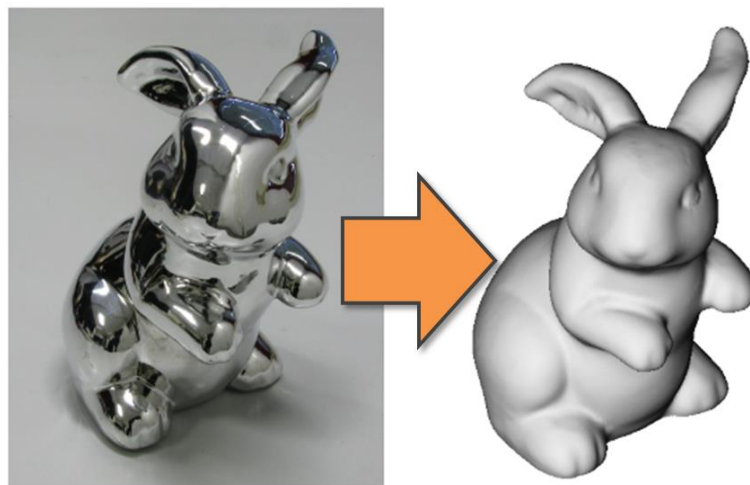


Figure 2: The novel multi-view normal field integration approach presented in [Weinmann et al. 2013] allows a dense reconstruction of mirroring objects with complex surface geometry.

---

### 3 APPENDIX

The following pages contain all the publications listed in section 1.2 that are directly linked to this deliverable. Other publications referenced in this deliverable can be found on the public Harvest4D webpage.

# 3D Scene Flow Estimation with a Piecewise Rigid Scene Model

Christoph Vogel · Konrad Schindler · Stefan Roth

**Abstract** 3D scene flow estimation aims to jointly recover dense geometry and 3D motion from stereoscopic image sequences, thus generalizes classical disparity and 2D optical flow estimation. To realize its conceptual benefits and overcome limitations of many existing methods, we propose to represent the dynamic scene as a *collection of rigidly moving planes*, into which the input images are segmented. Geometry and 3D motion are then jointly recovered alongside an over-segmentation of the scene. This piecewise rigid scene model is significantly more parsimonious than conventional pixel-based representations, yet retains the ability to represent real-world scenes with independent object motion. It, furthermore, enables us to define suitable scene priors, perform occlusion reasoning, and leverage discrete optimization schemes toward stable and accurate results.

Assuming the rigid motion to persist approximately over time additionally enables us to incorporate multiple frames into the inference. To that end, each view holds its own representation, which is encouraged to be consistent across all other viewpoints and frames in a temporal window. We show that such a *view-consistent multi-frame scheme* significantly improves accuracy, especially in the presence of occlusions, and increases robustness against adverse imaging conditions. At the time of writing (August 2014) our method achieves leading performance on the KITTI benchmark, for both flow and stereo.

**Keywords** 3D Scene Flow · Stereo · Motion Estimation · Piecewise Planarity · Piecewise Rigidity · Segmentation

---

Christoph Vogel · Konrad Schindler  
Photogrammetry & Remote Sensing, ETH Zurich  
Zürich, Switzerland  
E-mail: {vogel,konrad.schindler}@geod.baug.ethz.ch

Stefan Roth  
Department of Computer Science, TU Darmstadt  
Darmstadt, Germany  
E-mail: sroth@cs.tu-darmstadt.de

## 1 Introduction

The scene flow of a dynamic scene is defined as a dense representation of the 3D shape and its 3D motion field. Scene flow estimation aims to extract this information from images captured by two (or more) cameras at two (or more) different time instants. Applications that benefit from knowing the scene flow include 3D video generation for 3D-TV (Hung et al, 2013), motion capture (Courchay et al, 2009; Park et al, 2012; Vedula et al, 1999), and driver assistance (e.g., Müller et al, 2011; Rabe et al, 2010; Wedel et al, 2008). The 3D scene flow can be seen as a combination of two classical computer vision problems – it generalizes optical flow to 3D, or alternatively, dense stereo to dynamic scenes.

While progress in dense binocular stereo (Bleyer et al, 2011b; Hirschmüller, 2008; Yamaguchi et al, 2012, etc.) and optical flow (Brox et al, 2004; Sun et al, 2010; Unger et al, 2012, among others) has been both steady and significant over the years, the performance of 3D scene flow algorithms (e.g., Basha et al, 2010; Huguet and Devernay, 2007; Wedel et al, 2008) had been lacking in comparison. Only recently, methods emerged (Vogel et al, 2013b, 2014; Yamaguchi et al, 2014) that could leverage the additional information present in stereo video streams and outperform their dedicated two-dimensional counterparts at their respective tasks.

This may seem surprising, because 3D scene flow has a lot of commonalities with stereo and optical flow. This includes some of the principal difficulties, for example matching ambiguities due to insufficient evidence from the local appearance, or the aperture problem (more precisely a 3D version of it). Therefore, 3D scene flow estimation similarly requires prior assumptions about geometry and motion. A recent trend in both stereo and optical flow is to move away from simple pixelwise smoothness priors, as they have been found limiting. More expressive priors have been introduced, for example, by virtue of an over-parameterization (Nir et al, 2008), layered (Sun et al, 2010) or piecewise pla-

nar scene models (Bleyer et al, 2011b). In contrast, there has been relatively little work on using advanced priors in scene flow estimation. One exception is a regularizer that promotes local rigidity (Vogel et al, 2011), a common property of realistic scenes, by penalizing deviations from it.

*Piecewise rigid scene model.* Our first contribution is to go one step further and represent dynamic scenes as a collection of *planar regions, each undergoing a rigid motion*. Following previous work in stereo (Bleyer et al, 2011b), we argue that most scenes of interest consist of regions with a consistent motion pattern, into which they can be segmented. Consequently, we aim to jointly recover an implicit (over-)segmentation of the scene into planar, rigidly moving regions, as well as the shape and motion parameters of those regions (see Fig. 1). As we will show, such a parsimonious model is well-suited for many scenes of interest: The approximation holds well enough to capture the shape and motion of many real-world scenarios accurately, including scenes with independent object motion, while the stronger regularization affords stability. At the same time, reasoning in terms of rigid planar regions rather than pixels drastically reduces the number of unknowns to be recovered. Thereby, we additionally address the challenge of optimization or inference, one of the other principal difficulties that 3D scene flow shares with stereo and optical flow.

We (implicitly) represent 3D scene flow by assigning each pixel to a *rigidly moving 3D plane*, which has 9 continuous degrees of freedom (3 plane parameters, 6 motion parameters). To bootstrap their estimation, we start not from individual pixels, but from an initial superpixel segmentation of the scene. Based on the superpixels we compute a large, but finite set of candidate (moving) planes, and cast scene flow estimation as a *labeling problem*. The inference thus assigns each pixel to one of the segments (superpixels), and each segment to one of the candidate moving planes. We split the optimization into two steps. First, we find the best moving plane for each segment; reasoning on this coarser level captures long-range interactions and significantly simplifies and stabilizes the inference. Second, we go back to the pixel level and reassign pixels to segments; this step cleans up inaccuracies of the segmentation, whose initial boundaries were generated without taking the previously unknown surface or motion discontinuities into account.

*View-consistent multi-frame scene flow.* Our second contribution is to exploit this piecewise rigid scene model to overcome two limitations of existing scene flow techniques. We begin by observing that (i) there is no conceptual reason for a privileged reference view (e.g., Basha et al, 2010; Rabe et al, 2010; Valgaerts et al, 2010; Vogel et al, 2011; Wedel et al, 2008), as systematic challenges in imaging (specular reflections, occlusions, noise, lack of contrast, etc.) affect all



**Fig. 1** Example scene from Vaudrey et al (2008): Jointly estimated 3D geometry, 3D motion vectors, and superpixel boundaries, rendered from a different viewpoint.

frames, but not necessarily equally. Thus parameterizing the model w.r.t. a single viewpoint may in fact ignore important evidence present in other views (c.f. Fig. 2); (ii) data usually comes in the form of a stereo video sequence, and it appears wasteful not to exploit longer time intervals, especially in light of the first observation.

We go on to show that our piecewise planar and rigid scene model can be extended to simultaneously estimate geometry and 3D motion *over longer time intervals*, and to ensure that the estimate is *consistent across all views* within the considered time window. To that end we simultaneously parameterize the scene flow w.r.t. all views. While it may not be surprising that considering longer sequences may help motion estimation, at least in classical 2D optical flow estimation multi-frame extensions have largely not had the desired effect; two-frame methods are still the state of the art (see Baker et al, 2011; Geiger et al, 2012). We argue that long-term constraints may be more helpful in scene flow, since the representation resides in 3D space, rather than in a 2D projection. Constraints caused by physical properties, such as inertia, remain valid in the long term, and can be exploited more directly.

To make the estimate consistent across all views from a longer sequence, we constrain the segmentation to remain stable over time, enforce coherence of the representation between different viewpoints, and integrate a dynamic model that favors *constant velocity of the individual planes*. We empirically found this assumption to be valid as long as segments and temporal windows do not get too large.

*Contributions.* The main features of our proposed approach are: (i) A novel scene flow model that represents the scene with piecewise planar, rigidly moving regions in 3D space, featuring regularization between these regions and explicit occlusion reasoning; (ii) a view-consistent model extension that leads to improved results in challenging scenarios, by simultaneously representing 3D shape and motion w.r.t. every

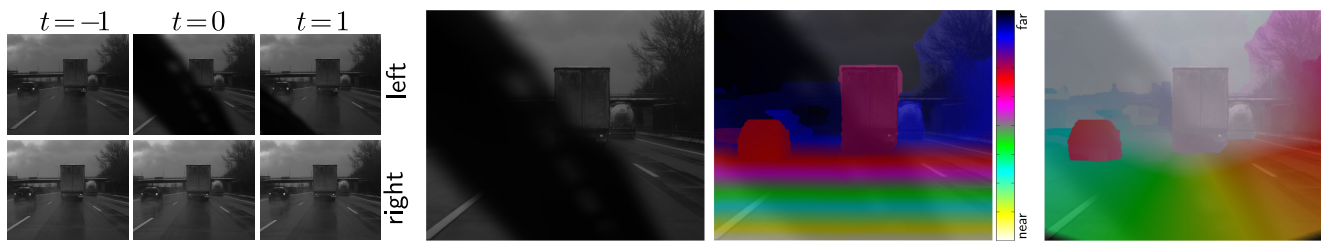


**Fig. 2** Consistency over multiple frames makes scene flow estimation robust against severe disturbances like the windscreen wiper. (*left*) Input frames. (*center left*) The left view at time  $t = 0$ . (*right*) Our scene flow estimate for that viewpoint (shown, from left to right, as disparity and reprojected 2D flow field).

image in a time interval, while demanding consistency of the representations; *(iii)* a multi-frame extension that yields a temporally consistent piecewise-planar segmentation of the scene and favors constant 3D velocity over time; and *(iv)* a clean energy-based formulation capturing all these aspects, as well as a suitable discrete inference scheme. The formulation can – at least conceptually – handle any number of viewpoints and time steps.

We demonstrate the advantages of our model using a range of qualitative and quantitative experiments. On particularly hard qualitative examples, our model turns out to be remarkably resistant to missing evidence, outliers, and occlusions. As a quantitative testbed we evaluate our method on the challenging KITTI dataset of real street scenes, using both stereo and flow benchmarks. In both benchmarks we achieve leading performance, even beating methods that are designed for the specific situation in the benchmark. At the time of writing (August 2014) our full (view-consistent multi-frame) model is the top performing method for both optical flow and stereo, when evaluated on full images including occlusion areas.

The present paper is based on two conference publications (Vogel et al, 2013b, 2014). We here describe the approach in greater detail, including the model itself, the inference scheme, proposal generation, and technical issues of occlusion reasoning. Moreover, we present a deeper analysis and more detailed comparison between the conventional parameterization and the view-consistent model, an experimental investigation of different optimization strategies, and study the influence of parameters on the quantitative results.

## 2 Related Work

Vedula et al (1999) first defined scene flow as the collective estimation of dense 3D geometry and 3D motion from image data. Their approach operates in two steps. After computing independent 2D optical flow fields for all views of the scene, the final 3D flow field is fit to the 2D flows, thus neglecting the image data in this step. Similarly, Wedel et al (2008) and Rabe et al (2010) proceed sequentially on the data of a calibrated stereo camera system. Starting from a precom-

puted disparity map, optical flow for a reference frame and disparity difference for the other view are estimated. Possibly the first to calculate geometry and flow jointly in a two-view setup were Huguet and Devernay (2007), addressing the problem in a variational formulation. The problem was generalized by Valgaerts et al (2010) to work with an unknown relative pose between the cameras, solely assuming knowledge of the camera intrinsics. They alternate scene flow calculation with estimating the relative camera pose. Operating entirely with 2D entities, these approaches partially neglect the 3D origin of the data. In particular, the proposed 2D regularizer encourages smooth projections, but not necessarily smooth 3D scene flow.

In contrast, Basha et al (2010) choose a 3D parameterization by depth and a 3D motion vector w.r.t. a reference view and estimate all parameters jointly, extending the popular optical flow method of Brox et al (2004) to scene flow. Arguing that a total variation prior on the 3D motion field is biased for realistic baselines, Vogel et al (2011) propose a regularizer that encourages locally rigid motion. Our model also employs a local rigidity assumption, but here we explicitly identify regions with a consistent motion pattern, into which the image is segmented.

The history of local rigidity priors dates back at least to Adiv (1985), who employed this assumption for sparse motion estimation. The idea was later extended to sparse scene flow by Carceroni and Kutulakos (2002). In a similar manner, Devernay et al (2006) extend the Lucas-Kanade technique (1981) to multi-camera scene flow and track planar, rigidly moving regions in 3D over several frames. While the scene representation of Carceroni and Kutulakos (2002); Devernay et al (2006) is similar to ours, there the regions move independently without interaction imposed by a global objective. Furukawa and Ponce (2008) go one step further and use the locally tracked rigid patch motion as input for a global optimization step, where the connectivity is defined by an explicit surface model, thus limiting admissible scenes to a fixed topology. 3D rigid body motions are further exploited in the context of scene flow estimation from RGB-D data by Hornacek et al (2014). They do not need to assume local surface planarity, but exploit the additional information

from the depth sensor and use a local rigidity prior to overcome large displacements. For computing optical flow, Nir et al (2008) over-parameterize the 2D flow field and explicitly search for rigid motion parameters, while encouraging their smoothness.

Most previous dense 3D scene flow methods have in common that they penalize deviations from spatial smoothness in a robust manner. Explicit modeling of discontinuities by means of segmentation or layer-based formulations has a long history in the context of stereo (Tao and Sawhney, 2000) and optical flow (Black and Jepson, 1996; Wang and Adelson, 1994). Wang and Adelson (1994) start from optical flow and define the regions by k-means clustering, where cluster centers are affine motions. Given an initial segmentation Black and Jepson (1996) similarly obtain a parametric model for each image region, which is then used as an additional constrain a final optical flow computation, thus the model allows for violations of the parametric model. These ideas recently gained renewed attention, however modern methods do not hold the segmentation or motion fixed, but rather infer or refine segmentation together with the scene parameters. Bleyer et al (2010, 2011b) segment the scene into planar superpixels and estimate disparity by parameterizing their geometry. Additionally penalizing deviations from an initial solution, segment-based stereo is also promoted by Yamaguchi et al (2012). More recently, this method was extended to epipolar flow (Yamaguchi et al, 2013) and epipolar scene flow (Yamaguchi et al, 2014), both assuming that the flow fulfills epipolar geometry constraints, *i.e.* is the result of pure camera ego-motion. General 2D optical flow is computed by Unger et al (2012), who parameterize the motion of each segment with 2D affine transformations, and also allow for occlusion handling. Aside from estimating 2D and not 3D motion, the method differs in the sense that no inter-patch regularization is performed, such that motion fields of adjacent segments are estimated completely independently of one another. Ju et al (1996) integrate segmentation and motion estimation in a different manner. Starting from regularly spaced, non-overlapping regions the optical flow in each region is described by multiple affine motions, *motion layers*. Similarly to our proposed spatial regularization, inter-segment constraints are imposed, here between layers across segment boundaries. Because motion layers can interact and thus influence their parametric representation, a segmentation into regions with similar motion is obtained implicitly.

Murray and Buxton (1987) were among the first to perform motion estimation over multiple frames. The admissible 2D optical flow fields are, however, limited to only small displacements. Black and Anandan (1991) instead encourage the similarity between the current and the past flow estimates, extrapolating motion fields from previous frames. While allowing for larger displacements, information is only

processed in a feed-forward fashion, in particular the present cannot influence the past. Much later, assuming a constant 2D motion field, Werlberger et al (2009) jointly reason over three consecutive frames. By considering constant 3D scene flow over time, we are able to address more general scenes. This constant velocity constraint is relaxed by Volz et al (2011), who encourage first and second order smoothness of the motion field as soft constraints. The motion is parameterized w.r.t. a single reference frame, thus reasoning about occlusion regions or outliers appears hard to achieve. Irani (2002) operates on much longer time intervals and enforces the estimated 2D motion trajectories to lie in a (rigid) subspace. Similarly, Garg et al (2013) require the 2D motions to lie in a low-rank trajectory space, but instead can use the prior as a soft constraint. Sun et al (2010, 2013) argue that the scene structure is more likely to persist over time than any motion pattern, hence avoid temporal smoothing at all, and instead jointly estimate the flow together with a segmentation into a small number of layers while requiring the pixel-to-layer membership to be constant. With the primary goal of high-level motion segmentation, Schoenemann and Cremers (2008) operate in a similar way: A video is segmented into several motion layers with long-term temporal consistency. Optionally, a 2D parametric motion for each layer is estimated as well. Our view-consistent formulation makes a related assumption, since we group pixels into planar and rigidly moving segments, while enforcing consistency of the segmentation over multiple frames. In contrast to motion layers, this much more fine-grained representation with hundreds of small segments enables us to address a wider range of scenes.

An explicit representation of 3D motion and shape allows scene flow methods to exploit temporal consistency over longer time intervals in a more straightforward manner, since smoothness constraints are better supported in the 3D scene than in its 2D projection. Rabe et al (2010) take advantage of this fact and propagate geometry and 3D motion across frames with the help of a Kalman filter. At each pixel the measurement vector for the filter is composed of scene flow vectors from the current and the previous frame, which are estimated with the method of Wedel et al (2008). Compared to its input, the filtered 3D motion and geometry contains significantly fewer outliers. Hung et al (2013) concatenate frame-to-frame stereo and flow to longer motion trajectories, which are, after passing several plausibility tests, included into the final optimization as soft constraints, similar to including feature matches in two-frame optical flow (Brox and Malik, 2011). The method advocates to propagate information through the whole sequence and, therefore, cannot output the scene flow without significant temporal delay, as is needed for several application scenarios. In their multi-camera setup Park et al (2012) also operate sequentially. Scene flow is first estimated frame-by-

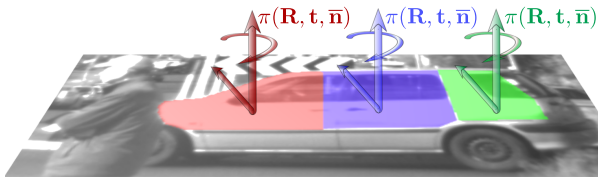


**Fig. 3** Schematic sketch of our scene representation: The scene is modeled as a collection of rigidly moving planar segments, here three different segments cover the side of a car.

frame and then smoothed over time by tensor voting. Courchay et al (2009) go further and represent the scene with an explicit deformable 3D mesh template, which is fitted to the video data from multiple cameras over 10–60 frames. The method is theoretically elegant, but computationally expensive. Both approaches target motion capture in controlled settings.

Techniques that avoid an arbitrary reference frame and instead treat all views equally are predominantly used in stereo. The simplest form is the widespread left-right consistency check (e.g., Hirschmüller, 2008) during post-processing. More recently, consistency tests were directly incorporated in the objective (Bleyer et al, 2011b). In our view-consistent formulation, we extend the latter strategy to scene flow, considering consistency across all images within a temporal window.

Introduced by Lempitsky et al (2008) for the case of 2D optical flow, fusion of different proposal sets has become a standard optimization technique. Here we employ such a scheme for the estimation of 3D scene flow.

### 3 Piecewise Rigid Model for 3D Scene Flow

To estimate 3D scene flow, we describe the dynamic scene as a collection of piecewise planar regions moving rigidly over time (Fig. 3). The motion and geometry of each region is governed by nine degrees of freedom, which we determine by minimizing a single objective function. During optimization, pixels are grouped into superpixels, and a suitable 3D plane and rigid motion is selected for each of these segments. Note that the implicitly obtained spatial segmentation does not aim to decompose the scene into semantic objects. Rather, an over-segmentation is desired to capture geometry and motion discontinuities, and to allow for the accurate recovery of non-planar and articulated objects. We begin our detailed description with the basic parameterization of the scene w.r.t. a single reference view and consider two time steps (Sec. 4). Later, we show how to achieve view-consistent scene flow over multiple frames (Sec. 5).

#### 3.1 Preliminaries and notation

We formalize our model for the classical case of images obtained by a calibrated stereo rig at two subsequent time steps. However, we note that an extension to a larger number of simultaneous views is straightforward. To distinguish between the different views, we use subscripts  $l, r$  to identify the *left* and *right* camera<sup>1</sup>, and superscripts  $t \in T = \{-1, 0, 1, \dots\}$  to indicate the acquisition time. We let the left camera at time  $t=0$  define a common coordinate system and refer to it as the *canonical* view; this simplifies the notation. This canonical view, on one hand, serves as an evaluation basis, and on the other hand, coincides with the sole *reference* view, in case view consistency is not employed. These choices lead to the projection matrices  $(\mathbf{K}|\mathbf{0})$  for the left and  $(\mathbf{M}|\mathbf{m})$  for the right camera. For simplicity, we assume *w.l.o.g.* the calibration matrix  $\mathbf{K}$  to be identical for both cameras.

In our model a 3D moving plane  $\pi \equiv \pi(\mathbf{R}, \mathbf{t}, \bar{\mathbf{n}})$  is governed by nine parameters, composed of a rotation matrix  $\mathbf{R}$ , a translation vector  $\mathbf{t}$ , and a scaled normal  $\bar{\mathbf{n}}$ , each with three degrees of freedom. Note that we do not explicitly distinguish between camera ego-motion and independent object motion, but describe the full motion in one forward time step. Later, when we extend our model to reason over multiple frames, we show how to cope with high frequent ego-motion of the camera (Sec. 5.3). In case of a single reference view, we assume all planes to be visible in the canonical view. Thus, as the canonical camera center and coordinate origin coincide, no visible plane can pass the origin. We can then define the scaled normal  $\bar{\mathbf{n}} \equiv \bar{\mathbf{n}}_l^0$  via the plane equation  $\mathbf{x}^\top \bar{\mathbf{n}} = 1$ , which holds for all 3D points  $\mathbf{x}$  on the plane. Throughout the paper it is convenient to transfer the moving plane also into other views and their respective camera coordinate systems. The plane equation still has to be valid after any rigid transformation, hence the scaled normal transforms in correspondence with 3D points  $\mathbf{x}$  on the plane  $\bar{\mathbf{n}}_l^0$ . For example, for the left camera at time step  $t=1$  the normal  $\bar{\mathbf{n}}_l^1$  in the respective coordinate system is found as:

$$\mathbf{x}^\top \bar{\mathbf{n}}_l^0 = 1 \Leftrightarrow (\mathbf{R}\mathbf{x} + \mathbf{t})^\top \bar{\mathbf{n}}_l^1 = 1 \Leftrightarrow \bar{\mathbf{n}}_l^1 = \frac{\mathbf{R}\bar{\mathbf{n}}_l^0}{1 + \mathbf{t}^\top \mathbf{R}\bar{\mathbf{n}}_l^0}. \quad (1)$$

We can, furthermore, determine the depth  $d$  observed at a pixel  $\mathbf{p}$  of the image  $I_v^t$ , acquired at time  $t$  w.r.t. the center of camera  $v$  through the inverse scalar product:

$$d(\mathbf{p}, \bar{\mathbf{n}}_v^t(\pi)) = \langle \mathbf{K}^{-1}\mathbf{p}, \bar{\mathbf{n}}_v^t(\pi) \rangle^{-1}. \quad (2)$$

This information is later needed to test for occlusions (Sec. 4.7), as well as to check the geometric consistency (Sec. 5.2) of the representation.

<sup>1</sup> “Left” and “right” are only used for intuition and do not necessarily correspond to the geometric configuration of the rig.

Utilizing a planar scene representation allows to map pixel locations conveniently to their corresponding positions from one view to another. In particular, a moving plane  $\pi$  induces homographies from the canonical view  $I_l^0$  to the other views given by:

$${}^0\mathbf{H}_r^0(\pi) = (\mathbf{M} - \mathbf{m}\bar{\mathbf{n}}^\top)\mathbf{K}^{-1} \quad (3a)$$

$${}^l\mathbf{H}_l^1(\pi) = \mathbf{K}(\mathbf{R} - \mathbf{t}\bar{\mathbf{n}}^\top)\mathbf{K}^{-1} \quad (3b)$$

$${}^l\mathbf{H}_r^1(\pi) = (\mathbf{M}\mathbf{R} - (\mathbf{M}\mathbf{t} + \mathbf{m})\bar{\mathbf{n}}^\top)\mathbf{K}^{-1}. \quad (3c)$$

Concatenating the transformations above, mappings between arbitrary view pairs can be obtained. This is achieved by first transforming back to the canonical view and then into the desired frame, *e.g.*  ${}^l\mathbf{H}_r^1(\pi) = {}^l\mathbf{H}_r^1(\pi) \cdot {}^0\mathbf{H}_l^1(\pi)^{-1}$ . For notational convenience we define  ${}^0\mathbf{H}_l^0(\pi)$  to be the identity, which maps the canonical frame onto itself.

#### 4 Single Reference View

For now our aim is to determine depth and 3D motion for every pixel of the designated reference view  $I_l^0$ . To that end, we formally define an energy function  $E(\mathcal{P}, \mathcal{S})$  over two mappings: a mapping  $\mathcal{S} : I_l^0 \rightarrow S$  that assigns each pixel of the reference view  $\mathbf{p} \in I_l^0$  to a segment  $s \in S$ ; and a mapping  $\mathcal{P} : S \rightarrow \Pi$  to select a 3D moving plane  $\pi \in \Pi$  from a pre-defined set of proposals  $\Pi$  for each of the segments  $s \in S$ . To find these mappings, we aim to minimize a single energy consisting of four terms:

$$E(\mathcal{P}, \mathcal{S}) = E_D(\mathcal{P}, \mathcal{S}) + \lambda E_R(\mathcal{P}, \mathcal{S}) + \mu E_S(\mathcal{S}) + E_V(\mathcal{P}, \mathcal{S}). \quad (4)$$

The data term  $E_D$  measures photo-consistency across the four views of our basic model. The regularization term  $E_R$  encourages (piecewise) smoothness of geometry and motion at segment boundaries. The boundary term  $E_S$  evaluates the quality of the spatial segmentation, encouraging a compact and edge-preserving over-segmentation of the reference image. The visibility term  $E_V$  deals with missing correspondences from areas that move out of the viewing frustum (out of bounds). The energy is then minimized in two steps: Starting with a fixed initial over-segmentation  $\mathcal{S}$ , we establish the link between segments and 3D moving planes, labeling each segment  $s \in S$  to belong to one of the moving planes  $\pi \in \Pi$ . Subsequently, we operate with a fixed mapping  $\mathcal{P}$  and re-assign each pixel  $\mathbf{p} \in I_l^0$  to one of the segments and, thereby, associated 3D moving planes. Note that the basic form of the energy remains the same when considering view consistency in Sec. 5.

#### 4.1 Data term

In its traditional role, the data term embodies the assumption that corresponding points in different views have similar appearance. Here, we achieve this through four constraints per pixel, two for the stereo pairs at time steps 0 and 1, and two optical flow constraints, one for each camera (see Fig. 4, left). Denoting the 3D moving plane at a pixel  $\mathbf{p}$  as  $\pi_{\mathbf{p}} = \mathcal{P}(\mathcal{S}(\mathbf{p}))$  and utilizing the homographies defined in Eq. (3), we can define stereo data terms between the cameras as

$$D_t^s = \sum_{\mathbf{p} \in I_l^0} \rho({}^0\mathbf{H}_l^t(\pi_{\mathbf{p}})\mathbf{p}, {}^0\mathbf{H}_r^t(\pi_{\mathbf{p}})\mathbf{p}), \quad t \in \{0, 1\}, \quad (5)$$

and optical flow data terms across time as

$$D_i^f = \sum_{\mathbf{p} \in I_l^0} \rho({}^0\mathbf{H}_i^0(\pi_{\mathbf{p}})\mathbf{p}, {}^0\mathbf{H}_i^1(\pi_{\mathbf{p}})\mathbf{p}), \quad i \in \{l, r\}. \quad (6)$$

The corresponding pixel location in a different view is usually a sub-pixel coordinate, hence image intensities are obtained via bilinear interpolation. For increased robustness in general conditions (*e.g.*, outdoors), we utilize the census transform  $\rho = \rho_C$  (Zabih and Woodfill, 1994) over a  $7 \times 7$  neighborhood to assess photo-consistency. We scale the Hamming distances by  $1/30$ . Although we are not limited to this specific choice, all examples and results are generated with the census data cost, unless explicitly stated otherwise. The complete data term is given as the sum of the four terms in Eqs. (5) and (6):

$$E_D(\mathcal{P}, \mathcal{S}) = D_0^s + D_1^s + D_l^f + D_r^f. \quad (7)$$

#### 4.2 Spatial regularization of geometry and motion

In our scene representation, geometry and motion parameters are shared among all pixels within a segment, hence explicit regularization within a segment is not needed. We can thus focus on the segment boundaries. One important benefit over pixelwise regularizers (Basha et al, 2010; Vogel et al, 2011) is that our boundary regularizer does not have to be overly strong to significantly stabilize scene flow estimation. Moreover, it rather naturally deals with discontinuities, a key problem area of previous scene flow techniques (*e.g.*, Vogel et al, 2011). Since boundaries regularly occur within a single object due to the over-segmentation, our regularization term assumes piecewise smooth 3D geometry and motion.

We model shape and motion priors independently (given a segmentation), and define our regularizer  $E_R(\mathcal{P}, \mathcal{S})$  as the sum of a geometric term  $E_R^G(\mathcal{P}, \mathcal{S})$  and a term  $E_R^M(\mathcal{P}, \mathcal{S})$  to measure the regularity of the motion field.

For now assume that two adjacent pixels  $\mathbf{p}$  and  $\mathbf{q}$  are assigned to the moving planes  $\pi_{\mathbf{p}} = \mathcal{P}(\mathcal{S}(\mathbf{p}))$  and  $\pi_{\mathbf{q}} =$

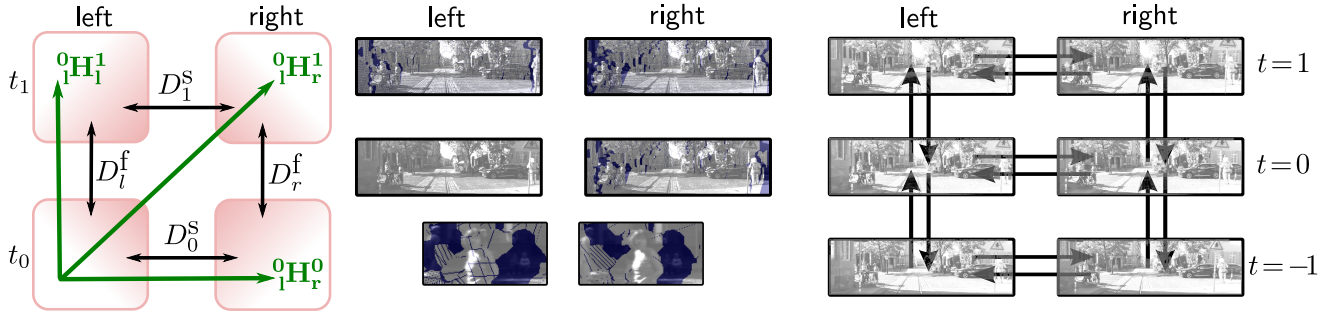


**Fig. 4** (left) Single reference-view model. Data terms (black arrows) and homographies (green). (center top) Pixels without correspondences when using a reference view (blue). Areas that are hard to match may be without correspondence in other views; view-consistency avoids this. (center bottom) Enlarged areas containing pixels without correspondence in the right camera. (right) Data terms in the three-frame view-consistent model: Consistency is encouraged for spatial and direct temporal neighbors (black arrows). All pixels of all views are considered in the energy.

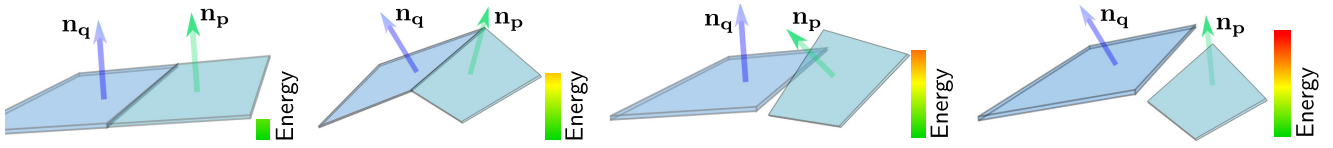


**Fig. 5** Schematic sketch of the geometric part of our regularizer: Smoothly connected regions (left) are favored over bending (center left). The more the situation degenerates, the higher the energy becomes (center right and right).

$\mathcal{P}(\mathcal{S}(\mathbf{q}))$ . We treat pixels as square patches, residing in the image plane in which they share a boundary. To measure the contribution to the regularization term along their common edge, we consider the (2D) endpoints of the edge between the pixels,  $c^1$  and  $c^2$ . We begin with the geometry term. By projecting the endpoints onto each of the two 3D planes, we obtain the 3D endpoints  $\mathbf{c}_p^1, \mathbf{c}_q^1, \mathbf{c}_p^2$  and  $\mathbf{c}_q^2$  (see Fig. 6). In case  $\mathbf{p}$  and  $\mathbf{q}$  lie on different planes, the pixel boundaries will, in general, not coincide in 3D space. We thus compute distance vectors between the 3D endpoints:  $\mathbf{d}_1 = \mathbf{c}_p^1 - \mathbf{c}_q^1$  and  $\mathbf{d}_2 = \mathbf{c}_p^2 - \mathbf{c}_q^2$ . Our goal is to penalize the distances along the shared edge. One could compute 3D distances for any point on the boundary in a similar fashion. However, since we are using planes as primitives, the 3D distance along the shared boundary in the image plane is simply a convex combination of the endpoint distances  $\|\alpha \mathbf{d}_1 + (1 - \alpha) \mathbf{d}_2\|$ .

To consider surface curvature we exploit this observation further and shift the 3D endpoints along their respective plane normals  $\mathbf{n}_p$  and  $\mathbf{n}_q$  before measuring distances. We denote the difference of the normals as  $\mathbf{d}_n = \mathbf{n}_p - \mathbf{n}_q$ , and define a distance function (see Fig. 6)

$$f_\gamma(\alpha, \beta) = \|\alpha(\mathbf{d}_1 + \gamma\beta\mathbf{d}_n) + (1 - \alpha)(\mathbf{d}_2 + \gamma\beta\mathbf{d}_n)\|. \quad (8)$$

The weight  $\gamma$  balances boundary distance vs. curvature. The geometry regularizer is then found by integration. Adding a factor  $3/2$  for mathematical convenience, we integrate the squared distance function  $(f_\gamma)^2$  along the boundary (w.r.t.

$\alpha$ ) and along the normal direction (w.r.t.  $\beta$ ) in closed form:

$$\begin{aligned} E_R^G(\mathcal{P}, \mathcal{S}) &= \sum_{(\mathbf{p}, \mathbf{q}) \in \mathcal{N}} w_{\mathbf{p}, \mathbf{q}} \psi \left( \frac{3}{2} \int_0^1 \int_{-1}^1 f_\gamma(\alpha, \beta)^2 d\beta d\alpha \right) \\ &= \sum_{(\mathbf{p}, \mathbf{q}) \in \mathcal{N}} w_{\mathbf{p}, \mathbf{q}} \psi \left( \|\mathbf{d}_1\|^2 + \|\mathbf{d}_2\|^2 + \langle \mathbf{d}_1, \mathbf{d}_2 \rangle + \gamma^2 \|\mathbf{d}_n\|^2 \right). \end{aligned} \quad (9)$$

The summation considers pixels to be adjacent in an (8-) neighborhood  $\mathcal{N}$ , where the length of the common edge is taken into account through the weight  $w_{\mathbf{p}, \mathbf{q}}$ , which can optionally also incorporate edge information (Eq. 13) of the image data.  $\psi(\cdot)$  denotes a (robust) penalty function. The intuition behind this form of regularization is shown in Fig. 5. Setting  $\gamma := 1$  our energy favors planar configurations over bending. By integrating squared distances of 3D vectors, the induced penalty increases smoothly as the situation degenerates. This soft transition helps in the realistic case of a limited proposal set of 3D moving planes  $\Pi$ .

The motion regularizer is obtained by first applying the rigid transformation to the moving planes. We then similarly integrate the endpoint distances  $\mathbf{d}_1^M = \mathbf{R}_p \mathbf{c}_p^1 + \mathbf{t}_p - \mathbf{c}_p^1 - (\mathbf{R}_q \mathbf{c}_q^1 + \mathbf{t}_q - \mathbf{c}_q^1)$ , as well as the differences between the (rotated) normals  $\mathbf{d}_n^M = (\mathbf{R}_p \mathbf{n}_p - \mathbf{n}_p) - (\mathbf{R}_q \mathbf{n}_q - \mathbf{n}_q)$ , leading to

$$\begin{aligned} E_R^M(\mathcal{P}, \mathcal{S}) &= \\ &= \sum_{(\mathbf{p}, \mathbf{q}) \in \mathcal{N}} w_{\mathbf{p}, \mathbf{q}} \psi \left( \|\mathbf{d}_1^M\|^2 + \|\mathbf{d}_2^M\|^2 + \langle \mathbf{d}_1^M, \mathbf{d}_2^M \rangle + \gamma^2 \|\mathbf{d}_n^M\|^2 \right). \end{aligned} \quad (10)$$

In both cases, robustness to discontinuities is achieved by employing truncated penalties  $\psi(y) = \min(\sqrt{y}, \eta)$  (with thresholds  $\eta_G, \eta_M$ ).

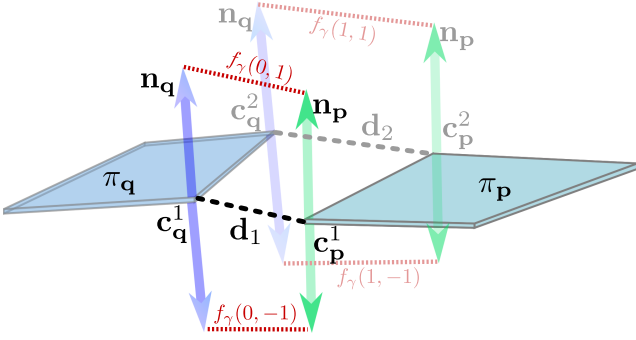


**Fig. 6** Illustration of the regularization scheme: The bilinear distance function  $f_\gamma$  considers geometric distance and curvature. Integrating the squared distances along the shared edge as well as along an extrusion of the normals leads to a closed form expression.

The proposed regularization scheme is not limited to 3D. For instance, the endpoint distances can be replaced by 2D entities such as the disparity difference, the difference between optical flow vectors, and the change of disparity over time. This is a popular choice for scene flow (Huguet and Devernay, 2007; Valgaerts et al. 2010) and (optionally) used here. Note, however, that falling back to 2D regularization can only yield a (close) approximation of the true 3D penalties, as projective foreshortening is not considered.

When reasoning at the segment level, we can approximate the regularizers by computing the penalties directly from the endpoints of the segments. By precomputing the length of the boundary (summing the edge weights along the shared border), the evaluation of the regularizer becomes much more efficient. Because superpixels in our framework are near-convex, the overall accuracy of the algorithm is barely affected (Fig. 12, right).

#### 4.3 Spatial regularization of the segmentation

Data term and spatial regularization operate not only on the segment-to-plane mapping  $\mathcal{P}$ , but also depend on the assignment of pixels to segments  $\mathcal{S}$ , which in our experience can lead to rather fragmented over-segmentations. To counteract this behavior and to incorporate prior knowledge that segments should be spatially coherent (but not necessarily connected) and preserve image edges, we add an additional regularization term, assessing the quality of the underlying segmentation:

$$E_S(\mathcal{S}) = \sum_{\substack{(\mathbf{p}, \mathbf{q}) \in \mathcal{N}(I_i^0), \\ \mathcal{S}(\mathbf{p}) \neq \mathcal{S}(\mathbf{q})}} u_{\mathbf{p}, \mathbf{q}} + \sum_{\mathbf{p} \in I_i^0} \begin{cases} 0, & \exists \mathbf{e} \in \mathcal{E}(s_i): \|\mathbf{e} - \mathbf{p}\|_\infty < N_S \\ \infty, & \text{else.} \end{cases} \quad (11)$$

The first term resembles a contrast sensitive pairwise Potts model, again evaluated over the (8-)neighborhood  $\mathcal{N}$  of a pixel. Here, the weight  $u_{\mathbf{p}, \mathbf{q}}$  allows to take into account the

image structure and the length of the edge between the pixels. To define these weights we follow Werlberger et al (2009) and apply the anisotropic diffusion tensor:

$$D^{\frac{1}{2}} = \exp(-\alpha|\nabla I|)gg^\top + g^\perp(g^\perp)^\top. \quad (12)$$

The image gradient direction  $g = \nabla I/|\nabla I|$  is determined via bicubic interpolation in the middle between  $\mathbf{p}$  and  $\mathbf{q}$ . Assuming  $I \in [0, 1]$ , we set  $\alpha = 5$  and define the weight

$$u_{\mathbf{p}, \mathbf{q}} := |D^{\frac{1}{2}} \vec{\mathbf{p}\mathbf{q}}|. \quad (13)$$

The second term links a segment to its seed point  $\mathbf{e} \in \mathcal{E}(s_i)$  in order to limit its maximum extent to a size smaller than  $(2N_S - 1) \times (2N_S - 1)$  pixels. This strategy prevents the scene flow from becoming overly simplified, but more importantly also restricts the number of candidate segments for a pixel, thus reducing the time needed for optimizing the energy w.r.t.  $\mathcal{S}$ . We found that a good strategy to define the seed points is to reuse the center of the original superpixels. Here we set  $N_S = 25$ , but values between 10 and 30 pixels perform alike (see Sec. 6.1). Note that a similar strategy was proposed by Veksler et al (2010) to compute an over-segmentation of a single image.

#### 4.4 Visibility term

So far we have not considered the problem of visibility, thus areas that fall *out of bounds*, *i.e.* are not visible in some of the images. Especially when dealing with large motions, these regions can cover a significant portion of the image. Configurations with no valid correspondence are not considered by the data term Eq. (7) and contribute 0 cost to the energy. Allowing for arbitrary moving planes in our model could, therefore, easily lead to a solution, where a significant portion of pixels is erroneously assigned a motion that moves them out of bounds. On the other hand, penalizing these kinds of configurations strongly could harm the results. Consider, for instance, a saturated region that actually moves out of bounds. A solution in which this region is mapped to a similarly saturated, but unrelated area in the other images lowers the data cost and would therefore be preferred. Since this regularly happens in challenging scenes, we address the problem as follows: Let us assume that we have access to an “oracle”  $V$ , which can predict whether a pixel will stay in the image or move *out of bounds*. Further, let  $V_l^1$ ,  $V_r^0$  and  $V_r^1$  be the predicted binary visibility masks for all but the reference image (*out-of-bounds*: 0, pixel visible: 1), and let  $\Gamma_i^j[\cdot]$  be a binary function that determines whether its argument lies within the boundaries of image  $I_i^j$ . We encourage the scene flow estimate to stay near that prediction, by defining

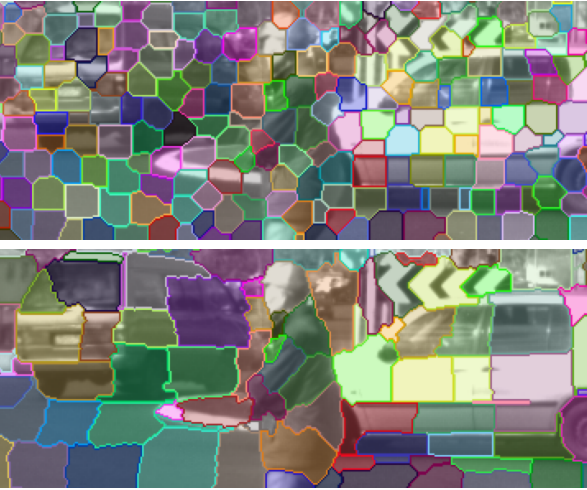


**Fig. 7** Demonstration of the per-pixel refinement: (*top*) Initial superpixel segmentation. (*bottom*) Superpixel segmentation after optimization w.r.t.  $\mathcal{S}$ .

a visibility term that forms part of the energy in Eq. (4):

$$E_V(\mathcal{P}, \mathcal{S}) = \theta_{\text{ob}} \sum_{\mathbf{p} \in I^0} |V_r^0(\mathbf{p}) - \Gamma_r^0 [{}^0\mathbf{H}_r^0(\pi_{\mathbf{p}})\mathbf{p}]| + \quad (14)$$

$$|V_l^1(\mathbf{p}) - \Gamma_l^1 [{}^0\mathbf{H}_l^1(\pi_{\mathbf{p}})\mathbf{p}]| + |V_r^1(\mathbf{p}) - \Gamma_r^1 [{}^0\mathbf{H}_r^1(\pi_{\mathbf{p}})\mathbf{p}]|,$$

with  $\theta_{\text{ob}} := 0.5 \max(\rho_C)$  set to half the maximal data cost. In practice, we found that common stereo and variational flow methods can predict pixels moving out-of-bounds sufficiently reliably, and consequently reuse the output of the 2D stereo and optical flow algorithms from the proposal generation step (Sec. 4.6). An alternative visibility predictor could be the ego-motion of the stereo camera system.

#### 4.5 Approximate inference

Inference in our piecewise rigid model entails estimating the continuous 9-dimensional variables describing geometry and motion of each rigidly moving plane, and the discrete assignments of pixels to segments. By restricting the optimization to a finite set of proposal moving planes, the whole problem is transferred into a labeling problem in a discrete CRF. The benefit is two-fold: First, we can leverage robust discrete optimization techniques that cope well with complex energies, particularly here the fusion move framework of Lempitsky et al (2008, 2010). Second, occlusions are discrete events and can thus naturally be integrated in the objective (Sec. 4.7).

To bootstrap the process, we start with a fixed segmentation  $\mathcal{S}$  and optimize the energy w.r.t.  $\mathcal{P}$ , selecting a suitable moving plane for each segment from the proposal set. To obtain the initial superpixel segmentation, we simply minimize the segmentation energy  $E_S$  alone, and subsequently

split strongly non-convex segments. We alternatively tested a segmentation into regular grid cells. Interestingly, this simplistic initialization works almost as well (see Sec. 6.1). In either case, the seed points  $\mathcal{E}$  are selected as the central pixels of the initial segments. When solving for  $\mathcal{P}$  we need to consider the data, visibility, and regularization terms only. After we found a solution for  $\mathcal{P}$ , the mapping is kept fixed and the energy is optimized w.r.t.  $\mathcal{S}$ , reassigning the pixels to segments and, thereby, implicitly to moving planes (*c.f.* Fig. 7). Because the segment size is restricted to a maximal side length of  $N_S$  through Eq. (11), the pseudo-Boolean function (Lempitsky et al, 2008) representing the local energy has at most  $(2N_S - 1)^2$  variables, which makes the optimization efficient. Distant segments can even be expanded in parallel. We use a similar strategy when optimizing for  $\mathcal{P}$ : We locally restrict the validity of each moving plane proposal to cover only a certain expansion region in the scene. In practice, we found that a proposal should at least cover 100 of its closest neighboring segments and set the region size accordingly. This allows to test several proposals in parallel. Note that we can iterate the alternating optimization further, but observe no practical benefit.

General pseudo-Boolean energies are usually optimized with QPBO (Rother et al, 2007), which can also handle non-submodular energies, but does not guarantee a complete labeling when supermodular edges are present. One disadvantage compared to standard graph cuts, however, is that the instantiated graph has twice the number of nodes than the (pseudo-Boolean) energy has variables. For our (non-submodular) energy we can alternatively use the local submodular approximation proposed by Gorelick et al (2014). This has the advantage that conventional graph cuts can be used, which is usually faster than QPBO. We particularly use LSA-AUX, which for each  $\alpha$ -expansion replaces pairwise supermodular potentials by a local plane approximation that bounds the true energy from above. This idea is very simple to implement and delivers a significantly better approximation than a simple truncation of non-submodular terms. We experimentally compare both approaches in Sec. 6.

#### 4.6 Proposal generation

To perform inference over the 3D geometry and motion of the segments, we require an (initial) set of proposal planes together with their rigid motion. We can create these from either the output of other scene flow algorithms, or from a combination of stereo and optical flow methods. To convert the pixelwise correspondence information to our representation, we separately fit the parameters of a 3D plane and its rigid motion to each superpixel of the initial segmentation. Fitting is complicated by inaccuracies or noise in the stereo and flow estimates, and by superpixels that are not well-aligned with depth and motion discontinuities. We thus opt

for a robust procedure and minimize the transfer error integrated into a robust cost function, particularly the Lorentzian  $\phi(x) = \log(1 + \frac{x}{2\sigma^2})$ :

$$\sum_{\mathbf{p} \in s} \phi(\|P({}^0\mathbf{H}_r^0(\bar{\mathbf{n}})\mathbf{p}) - \mathbf{p}'\|^2) \rightarrow \min_{\bar{\mathbf{n}}} \quad (15a)$$

$$\sum_{\mathbf{p} \in s} \phi(\|P({}^0\mathbf{H}_l^1(\mathbf{R}, \mathbf{t})\mathbf{p}) - \mathbf{p}'\|^2) \rightarrow \min_{\mathbf{R}, \mathbf{t}}, \quad (15b)$$

where the dependence of the homographies on the parameters (the normal  $\bar{\mathbf{n}}$  and rigid motion  $(\mathbf{R}, \mathbf{t})$ ) is made explicit, and  $P$  denotes the conventional projection operator. Each pixel  $\mathbf{p}$  of segment  $s \in S$  is matched to its 2D correspondence  $\mathbf{p}'$ , determined by the proposal algorithm. We parameterize the rotation in Eq. (15b) by its exponential map to define the derivatives, and use the previously determined scaled normal to derive the homography (*c.f.* Eq. 3). After bootstrapping this non-convex optimization problem with simple iterated least squares, two iterations of the limited-memory Broyden-Fletcher-Goldfarb-Shanno algorithm (LM-BFGS) suffice for our purposes. The quality of the fit is analyzed in Sec. 6.1. Note that since we are treating the estimation of 3D planes and rigid motions independently, the problem of fitting a rigid motion is similar to the computation of the ego-motion of a stereo camera system, such that algorithms for this problem could also be applied (*e.g.*, Badino and Kanade, 2011). Here, however, we only consider the motion of an individual segment and not of the complete stereo rig.

#### 4.6.1 Additional proposals

The strategy of selecting parts of the solution from a set of proposals allows to include additional information in an unbiased way, without the need for altering the energy formulation. We exploit this property by including the estimated ego-motion of the stereo system as an additional proposal. The ego-motion is found by reusing our fitting procedure from above (Eq. 15b) on the segment centers and their correspondences, given by the output of our per-segment solution (obtained after optimizing w.r.t. the mapping  $\mathcal{P}$ ). We then can fuse the current solution with the estimated ego-motion.

Additionally, we use a *local replacement* strategy, motivated by proposal instances for which depth and motion errors are not correlated. We posit that these largely result from the 2D proposal algorithms, which estimate motion and depth independently. We address this with additional proposals: We randomly select proposals and propagate a part of their state to other segments in a 2-neighborhood. This can either be the geometry or the rigid motion, which simply replaces the corresponding state of the neighbors. This procedure is iterated several ( $\approx 4000$ ) times, leading to a combination of geometry and motion of neighboring segments. The strategy has similarities to the PatchMatch idea (Barnes et al, 2009; Bleyer et al, 2011a), as information is shared and distributed among neighboring segments.

#### 4.7 Occlusion handling

The data term as defined in Eq. (7) assumes that every pixel is visible; no occlusion reasoning takes place. Given our 3D scene representation, we can explicitly reason about occlusions. Compared to stereo, the handling of occlusions for scene flow has the advantage of having two (or more *c.f.* Sec. 5.3) additional views of the scene. Accordingly, pixels that are occluded in a subset of views may still be visible in one of the view pairs.

To leverage this, occlusion handling is applied to all pairs of views for which a data term is formulated. We formalize this only for a single view pair, because the mathematical formulation is equivalent for each summand of the data term. We make use of the well-known principle (dating back at least to Kolmogorov and Zabih, 2001) of applying a constant penalty  $\theta_{\text{occ}}$ , if a pixel is occluded in at least one of the two views of the pair. The penalty is chosen as  $\theta_{\text{occ}} := \theta_{\text{oob}}$  (Eq. 14). Although occlusions and out-of-bound areas have different causes, the impact on the correspondence is the same: The pixel correspondence cannot be judged by the appearance, and hence the data costs of Eqs. (5) or (6) are invalid. Note that pixels that are assigned to the same moving plane in our scene representation naturally cannot occlude each other.

To simplify the exposition, we will not present our occlusion model in its most general form, but rather one instantiation within a single fusion/expansion move of the approximate inference procedure from Sec. 4.5. Hence, we are dealing with a binary optimization problem. Assuming a fixed segment-to-plane mapping  $\mathcal{P}$ , we will first investigate the update of the per-pixel segmentation  $\mathcal{S}$ . Differences in the update procedure when solving for  $\mathcal{P}$  will be discussed later. *W.l.o.g.* let the binary state  $x_{\mathbf{p}} = 0$  denote that the pixel  $\mathbf{p}$  retains its current segment assignment and, accordingly,  $x_{\mathbf{p}} = 1$  indicate a switch to the trial segment  $\alpha$ . We begin by expressing the data term from Sec. 4.1 in the form of a pseudo-Boolean function:

$$D(\mathbf{x}) = \sum_{\mathbf{p} \in I^0} \left( u_{\mathbf{p}}^0 (1 - x_{\mathbf{p}}) + u_{\mathbf{p}}^1 x_{\mathbf{p}} \right), \quad (16)$$

where the vector  $\mathbf{x}$  denotes all binary pixel assignments. The data penalty equals  $u_{\mathbf{p}}^0$  if  $\mathbf{p}$  remains in its current segment, and  $u_{\mathbf{p}}^1$  if  $\mathbf{p}$  is assigned to segment  $\alpha$ .

Whether a pixel  $\mathbf{p}$  is occluded or not depends both on its binary segment assignment  $x_{\mathbf{p}}$ , and on whether there is any other pixel  $\mathbf{q}$  (or possibly multiple pixels) that occludes  $\mathbf{p}$ . Determining whether  $\mathbf{q}$  triggers an occlusion in turn depends on its segment assignment  $x_{\mathbf{q}}$ . With  $\mathcal{O}_{\mathbf{p}}^i$  we identify the set of all pixel-assignment pairs  $(\mathbf{q}, j)$ , for which pixel  $\mathbf{q}$  occludes pixel  $\mathbf{p}$  if  $x_{\mathbf{p}} = i$  and  $x_{\mathbf{q}} = j$ . Now we can replace Eq. (16)

with our occlusion-aware data term

$$D_O(\mathbf{x}) = \sum_{\mathbf{p} \in I_v^0} \left( \theta_{\text{occ}} + \sum_{i=0}^1 \hat{u}_{\mathbf{p}}^i [x_{\mathbf{p}} = i] \prod_{(\mathbf{q}, j) \in \mathcal{O}_{\mathbf{p}}^i} [x_{\mathbf{q}} \neq j] \right). \quad (17)$$

Here, we denote the difference of the (unoccluded) data penalty and the occlusion cost  $\theta_{\text{occ}}$  by  $\hat{u}_{\mathbf{p}}^i = u_{\mathbf{p}}^i - \theta_{\text{occ}}$ , and with  $[\cdot]$  the Iverson bracket. To facilitate a better understanding of the equation above, let us focus on a single pixel  $\mathbf{p}$ . The respective summand becomes  $\hat{u}_{\mathbf{p}}^0$ , if both  $x_{\mathbf{p}} = 0$  and the product equals to 1. The latter happens if no occlusion occurs, that is either all possibly occluding pixels  $\mathbf{q}$  are assigned to a segment  $x_{\mathbf{q}}$  in which they do not lead to an occlusion, or the set  $\mathcal{O}_{\mathbf{p}}^0$  is empty, meaning that no pixel exists that could possibly occlude  $\mathbf{p}$ . The data cost overall thus equals  $\theta_{\text{occ}}$  in case of an occlusion, and the standard data penalty  $u_{\mathbf{p}}^0$  or  $u_{\mathbf{p}}^1$ , otherwise.

Recall that we establish the segment-to-plane mapping  $\mathcal{P}$  by reasoning over entire segments (see Sec. 4.5). Therefore, we directly extend the occlusion model to the segment level. The potentials of the respective pseudo-Boolean energies in Eqs. (16) and (17) look the same, but with variables representing segments instead of pixels. We consider a segment to be (significantly) occluded if its central pixel is occluded. Because our segments are compact and similarly sized, at least one quarter of a segment has to be occluded by a different region to render the central pixel occluded. To check for occlusions we employ conventional z-buffering, utilizing Eq. (2) to compute the depth at each pixel.

Depending on the number of possibly occluding pixels, the (per-pixel) penalty may be a higher-order pseudo-Boolean function ( $|\mathcal{O}_{\mathbf{p}}^i| > 1$ ). Optimization techniques based on graph cuts, including QPBO, can only be applied to quadratic polynomials, which is why all higher-order terms have to be reduced to pairwise ones. Over the years several reduction techniques have been proposed (e.g., Ali et al, 2008; Ishikawa, 2009; Rother et al, 2009). Each applies a certain transformation that approaches the reduction independently for each higher order summand of the energy. We refrain from presenting these exhaustive details at this point and instead refer to the Appendix A.

## 5 View-Consistent Model

Equipped with our basic representation and model from Sec. 4, we now generalize it to estimate scene flow for all views and time instants simultaneously. A major benefit compared to using a single reference view is that the entire image evidence of all views has to be explained. This results in a more robust estimate, which is less prone to common imaging artifacts. Occlusion handling can be improved as well. Another benefit is that significantly fewer non-submodular edges occur in the pseudo-Boolean function constructed during the

optimization process. We defer details to the experimental evaluation. To enable a view-consistent model, we first need to extend the notion of the segmentation to all views, with the challenge of generating a consistent segmentation of the scene across views and time. An obvious downside of a view-consistent approach is a significantly enlarged set of unknowns, since the assignments from segments to moving planes and pixels to segments have to be computed for each involved view.

After establishing the concept of view-consistency, we aim to estimate scene flow for more than two time steps. We thus extend the idea of rigidity by assuming constant translational and rotational velocity of the 3D moving planes. Note that due to the short time intervals considered, this assumption is valid for many application scenarios. In the following, we start our description for only two time steps, and later explain how to extend our model to multiple frames in time.

### 5.1 Model overview

As before we strive to determine depth and a 3D motion vector for every pixel, but this time for all the views examined. We thus keep track of a superpixel segmentation in every view, denoted as  $S_v^t$ , the set of segments in the image  $I_v^t$  in view  $v$  at time step  $t$ . The energy definition (Eq. 4) is extended to be a function of two sets of mappings. The first set of mappings  $\mathcal{S} = \{\mathcal{S}_v^t : t, v\}$  with  $\mathcal{S}_v^t : I_v^t \rightarrow S_v^t$  assigns each pixel of frame  $I_v^t$  to a segment of  $S_v^t$ . With the second set  $\mathcal{P} = \{\mathcal{P}_v^t : t, v\}$ , a rigidly moving plane is selected for each segment in each view:  $\mathcal{P}_v^t : S_v^t \rightarrow \Pi$ . Recall that  $\Pi$  denotes a candidate set of possible 3D moving planes. The formal definition of the energy takes the same basic form as Eq. (4):

$$E^{\text{VC}}(\mathcal{P}, \mathcal{S}) = E_D^{\text{VC}}(\mathcal{P}, \mathcal{S}) + \lambda E_R^{\text{VC}}(\mathcal{P}, \mathcal{S}) + \mu E_S^{\text{VC}}(\mathcal{S}). \quad (18)$$

However, in our view-consistent setting the definition of the data term  $E_D^{\text{VC}}$  is significantly different, as not only photo-consistency w.r.t. a reference view is considered, but also the consistency of the underlying geometric configuration and segmentation of the scene. The regularization term  $E_R^{\text{VC}}$  and the segmentation term  $E_S^{\text{VC}}$  are straightforward extensions of their single view counterpart from Sec. 4. In our experience, by explaining the available evidence from all images, this view-consistent formulation does not require an explicit visibility term (Sec. 4.4).

The spatial smoothness assumption is extended to all views, simply summing the contributions of motion (Eq. 9) and geometry (Eq. 10) terms per frame:

$$E_R^{\text{VC}}(\mathcal{P}, \mathcal{S}) = \sum_{t \in T} \sum_{v \in \{l, r\}} E_R^G(\mathcal{P}_v^t, \mathcal{S}_v^t) + E_R^M(\mathcal{P}_v^t, \mathcal{S}_v^t). \quad (19)$$

In a similar fashion we extend the regularization of the segmentation (Eq. 11) to all considered views:

$$E_S^{\text{VC}}(\mathcal{S}) = \left( \sum_{t \in T, v \in \{l, r\}} \sum_{(\mathbf{p}, \mathbf{q}) \in \mathcal{N}(I_v^t), \mathcal{S}(\mathbf{p}) \neq \mathcal{S}(\mathbf{q})} u_{\mathbf{p}, \mathbf{q}} \right) + \sum_{\mathbf{p} \in I_v^0} \begin{cases} 0, & \exists \mathbf{e} \in \mathcal{L}(s_i): \|\mathbf{e} - \mathbf{p}\|_\infty < N_S \\ \infty, & \text{else,} \end{cases} \quad (20)$$

where  $\mathcal{N}$  is again defined as the 8-neighborhood. Note that the second term is only applied to the canonical view, such that the maximal size of a segment is only restricted in the canonical frame. Also note that we treat the segmentations of the different frames independently. However we encourage the segmentation to be consistent across views (*c.f.* Fig. 11) such that the restriction on the maximal segment size is also propagated to all other images<sup>2</sup>. Consistency between the superpixel segmentations is encouraged in the data term, described in the following.

## 5.2 View-consistent data term

In our view-consistent model we explicitly store a description of the scene in terms of moving planes as observed in each of the views. To exploit the redundancy in this representation, we check the consistency of the scene flow estimate in each view with its direct neighbors in time, as well as with the other views at the same time instant (Fig. 4, right). We here slightly abuse the term consistency: In its classical sense we check for photo-consistency of the images at corresponding pixel locations, determined through their assigned moving planes  $\pi \equiv \pi(\mathbf{R}, \mathbf{t}, \bar{\mathbf{n}})$ . However, in our novel scene representation we can also check the geometric configuration for plausibility, test for occlusions, and verify the consistency of the segmentation. This is done by comparing depth values induced by the respective moving plane (Eq. 2), based on the underlying image segmentation (see Fig. 8).

Now let us assume we want to check the consistency between a pixel location  $\mathbf{p} \equiv \mathbf{p}_v^t$  in view  $v$  at time  $t$  and its corresponding pixel location  $\hat{\mathbf{p}}_{\hat{v}}^{\hat{t}}$  in view  $\hat{v}$  at time  $\hat{t}$ . We denote the 3D moving plane of the pixel  $\mathbf{p}$  by  $\pi_{\mathbf{p}} = \mathcal{P}_v^t(\mathcal{S}_v^t(\mathbf{p}))$ . The related homography allows to determine the corresponding pixel location in the other view,  $\hat{\mathbf{p}}_{\hat{v}}^{\hat{t}} = {}_v^{\hat{t}}\mathbf{H}_{\hat{v}}^t(\pi_{\mathbf{p}})\mathbf{p}$ , and the depth function  $d(\mathbf{p}, \bar{\mathbf{n}}_v^t(\pi))$  from Eq. (2) enables evaluating the geometric configuration at that pixel. The data term for a single pixel  $\mathbf{p}$  in view  $v$  at time-step  $t$  assigned to the moving plane  $\pi_{\mathbf{p}}$  with the adjacent view  $\hat{v}$  at time-step  $\hat{t}$  is then given

by

$$\rho(\mathbf{p}, \hat{\mathbf{p}}_{\hat{v}}^{\hat{t}}) = \begin{cases} \theta_{\text{imp}} & \text{if } \frac{d(\hat{\mathbf{p}}_{\hat{v}}^{\hat{t}}, \bar{\mathbf{n}}_{\hat{v}}^{\hat{t}}(\pi_{\hat{\mathbf{p}}_{\hat{v}}^{\hat{t}}}))}{d(\hat{\mathbf{p}}_{\hat{v}}^{\hat{t}}, \bar{\mathbf{n}}_{\hat{v}}^{\hat{t}}(\pi_{\mathbf{p}}))} > 1 + \varepsilon \\ \theta_{\text{occ}} & \text{if } \frac{d(\hat{\mathbf{p}}_{\hat{v}}^{\hat{t}}, \bar{\mathbf{n}}_{\hat{v}}^{\hat{t}}(\pi_{\mathbf{p}}))}{d(\hat{\mathbf{p}}_{\hat{v}}^{\hat{t}}, \bar{\mathbf{n}}_{\hat{v}}^{\hat{t}}(\pi_{\hat{\mathbf{p}}_{\hat{v}}^{\hat{t}}}))} > 1 + \varepsilon \\ \theta_{\text{oob}} & \text{otherwise if } \hat{\mathbf{p}}_{\hat{v}}^{\hat{t}} \notin I_{\hat{v}}^{\hat{t}} \\ \rho_C(\mathbf{p}, \hat{\mathbf{p}}_{\hat{v}}^{\hat{t}}) + \theta_{\text{mvp}} & \text{otherwise if } \pi_{\mathbf{p}} \neq \pi_{\hat{\mathbf{p}}_{\hat{v}}^{\hat{t}}} \\ \rho_C(\mathbf{p}, \hat{\mathbf{p}}_{\hat{v}}^{\hat{t}}) & \text{otherwise.} \end{cases} \quad (21)$$

The first two cases are depicted in Fig. 8a and b. Here the relative difference in depth is used to distinguish between *implausible* and *occlusion* cases. This distinction is similar to comparing disparity values for the stereo case (Bleyer et al, 2011b). The first case (Fig. 8a) describes a geometrically implausible situation, in which the depth of the moving plane  $\pi_{\mathbf{p}}$ , observed from the 2<sup>nd</sup> camera in pixel  $\hat{\mathbf{p}}_{\hat{v}}^{\hat{t}}$ , is smaller than the depth assigned to the pixel in that 2<sup>nd</sup> view. In this situation the 3D point on the plane  $\pi_{\hat{\mathbf{p}}_{\hat{v}}^{\hat{t}}}$  would be occluded by the moving plane  $\pi_{\mathbf{p}}$  and not be visible by the 2<sup>nd</sup> camera. We apply a fixed penalty  $\theta_{\text{imp}}$  in this case. In the second case (see Fig. 8b), the depth of the moving plane  $\pi_{\mathbf{p}}$  is greater than that of the corresponding plane  $\pi_{\hat{\mathbf{p}}_{\hat{v}}^{\hat{t}}}$  and, therefore, the pixel  $\mathbf{p}$  is occluded in the second view. Again, a fixed penalty  $\theta_{\text{occ}}$  is applied. This concept of occlusion reasoning via cross checking the current solution among views is only possible by simultaneously estimating a solution for all views and rather different from the occlusion detection technique presented in Sec. 4.7 for a single reference view. An additional benefit is that the resulting energy function induces only pairwise edges. In Eq. (17), in contrast, multiple possible labels for the corresponding location in the other view may exist, which in turn leads to higher-order terms in the respective pseudo-Boolean energy. In our experience the view-consistent formulation leads to fewer supermodular edges in the optimization (see Sec. 6.2), resulting in a simpler optimization problem.

Since the set of proposal planes is limited due to practical considerations, we cannot assume that our representation always assigns a fully accurate depth for every pixel. Instead of strictly comparing relative depth values we, therefore, opt for a relaxed test by including the  $\varepsilon$  parameter, empirically set to  $\varepsilon := 0.015$ . This additionally alleviates aliasing artifacts introduced by the finite resolution of the pixel grid.

The third case penalizes pixels moving out of the viewing frustum (*out of bounds*) with a fixed penalty  $\theta_{\text{oob}}$ . By employing view consistency, the solution has to respect the information from all views of the scene. Hence the treatment of this event can be a lot simpler than in the case of a single reference frame, where an additional visibility term (Sec. 4.4) was included.

<sup>2</sup> this property is further exploited in the inference procedure

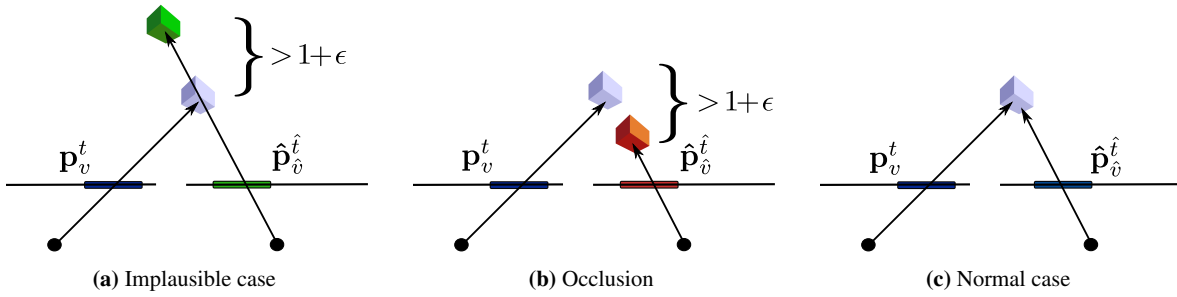


Fig. 8 Illustration of the per-pixel view-consistent data term (see text for more details).

When pixels are in geometric correspondence we apply the usual census data penalty  $\rho = \rho_C$  to measure photo-consistency (*c.f.* Sec. 4.1). In (Vogel et al, 2014) we originally proposed to additionally truncate the data term at half the maximal possible cost at a pixel ( $0.5 \max(\rho_C)$ ). An investigation of this particular choice shows that the number of resulting non-submodular terms in the optimization is reduced (Sec. 5.4), however some of the information is lost, which can lead to a decreased accuracy. Consequently, we avoid the truncation here.

If the pixels are in geometric correspondence, but belong to different moving planes, we assert a *moving plane violation* and impose an additional penalty  $\theta_{mvp}$ . This leads to the desired view-consistent segmentation, as pixels are encouraged to pick the same 3D moving plane in neighboring views.

In practice, it appears prudent to penalize pixels without correspondence equally, thus we set both penalties for occlusions and pixels moving out of bounds to  $\theta_{oob} = \theta_{occ} = 0.5 \max(\rho_C)$ . Aliasing again prevents us from penalizing implausible configurations with an infinite penalty; instead we set  $\theta_{imp} := \max(\rho_C)$ , which also prevents deadlocks in the optimization. While this can lead to a few implausible assignments in the final estimate, the overall error is reduced. For the same reasons we allow for deviations from our consistency assumption for the segmentation and empirically set  $\theta_{mvp} := 5/16 \theta_{oob}$ .

All views are treated equally in our model, thus the per-pixel contribution from Eq. (21) is summed over all pixels of all frames. Our data term consists of the summed data costs for all stereo pairs and frames that are direct neighbors in time (Fig. 4, right):

$$E_D^{VC}(\mathcal{P}, \mathcal{S}) = \sum_{t \in T} \sum_{v \in \{l, r\}} \sum_{\mathbf{p} \in I_v^t} \left( \sum_{\hat{\mathbf{v}} \neq v} \rho(\mathbf{p}, \hat{\mathbf{p}}_{\hat{\mathbf{v}}}^t) + \sum_{\substack{\hat{t} \in T \\ |\hat{t} - t| = 1}} \rho(\mathbf{p}, \hat{\mathbf{p}}_v^{\hat{t}}) \right). \quad (22)$$

In contrast to the reference-view formulation (*c.f.* Fig. 4, left), each view pair is considered twice by the data term, because every view holds its own scene flow representation.

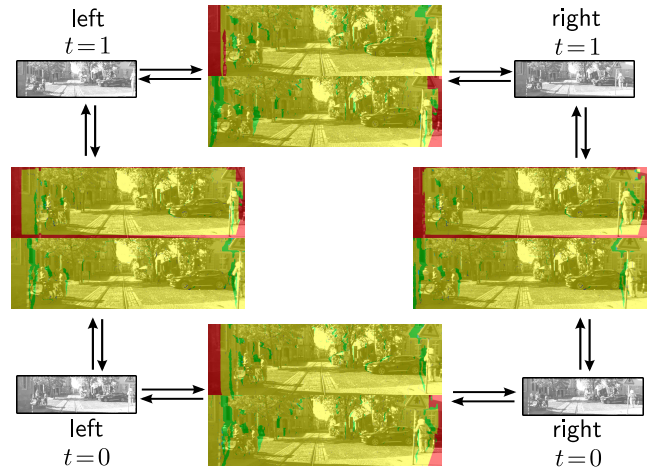
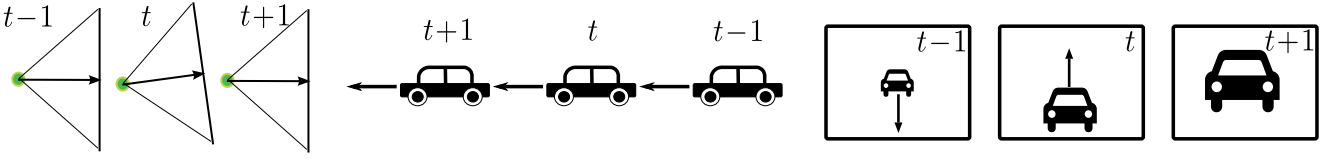


Fig. 9 Example from the KITTI training set (#191): Active data term  $\rho$  (Eqs. 21 and 22). Colors denote normal photo-consistency (yellow), out of bounds (red), occluded (green), moving plane violation (dark blue) and implausible (light blue) cases.

Fig. 9 illustrates the view-consistent data term. The internal states assigned by the data term (cases of Eq. 21) to each view pair are shown for each individual pixel.

### 5.3 View-consistent multi-frame extension

We now discuss the details of extending our view-consistent model to more than just two frames. As mentioned, geometry, motion and segmentation regularizers can be extended to a larger number of frames in a rather straightforward fashion (Eqs. 19 and 20). The data term however needs special consideration, as we need to define homographies between the additional views and also transform the normals into the specific view coordinate system. Recall that we restrict ourselves to reason only over shorter time intervals and thus can assume the motion of a moving plane to be of constant velocity in both its rotational and translational component. Under this condition suitable homographies can be found by a concatenation of the homographies defined in Eq. (3). Similarly, view-normals for the different time steps are generated by a repeated application of Eq. (1), thus again as-



**Fig. 10** Variation in camera pitch limits the validity of the constant velocity model: (left) A scene observed by a moving camera with varying pitch. (right) Camera images with induced 2D flow (black arrows). We compensate camera pitch by removing the ego-motion of the camera.

suming constant velocity. Note here, that the normals in the proposal set  $\Pi$  are always stored in the canonical coordinate system.

Such a model can tolerate small deviations from this constant 3D velocity assumption in the scene, but this is put to a test if the camera system itself is violating this assumption. Especially abrupt rotational changes in the viewing direction affect the whole image of the scene. The automotive application in our experiments is a good example for this. Scene flow estimation is challenged by a common high-frequent pitching motion of the stereo rig, often caused by an unsteady road surface and amplified by the suspension of the vehicle. In our model the motion is encoded relative to the respective camera coordinate system, such that even slight changes in the relative camera position can induce significant changes in the relative geometry and motion (Fig. 10). To address this problem, we introduce the following extension, in which we include ego-motion estimates for the different time steps.

First, we compute the relative ego-motion  $\mathbf{E}^t = [\mathbf{Q}^t | \mathbf{s}^t]$  between all consecutive time steps  $t$  and  $t+1$ . The computation of homographies between successive frames then proceeds by first applying the motion induced by the moving plane representation with the ego-motion part removed, and then the relative ego-motion from time step  $t$  to  $t+1$ . Recall that the rotation  $\mathbf{R}$  and the translation  $\mathbf{t}$  of a moving plane are stored in the coordinate system of the canonical view, thus unaware of any ego-motion. Then we can remove the relative ego-motion of the canonical view  $\mathbf{E}^0$  by applying  $(\mathbf{E}^0)^{-1} = [(\mathbf{Q}^0)^{-1} | -(\mathbf{Q}^0)^{-1}\mathbf{s}^0]$ .

As an example, the homography between the frames  $t$  and  $t+1$  in the left view becomes

$${}^t\mathbf{H}_l^{t+1}(\pi) = \mathbf{K} \left( \mathbf{Q}^t (\mathbf{Q}^0)^{-1} \mathbf{R} - (\mathbf{Q}^t (\mathbf{Q}^0)^{-1} (\mathbf{t} - \mathbf{s}^0) + \mathbf{s}^t) (\bar{\mathbf{n}}_l^t)^\top \right) \mathbf{K}^{-1}. \quad (23)$$

Further note the use of the corrected view normal in Eq. (23), for which we can find a similar expression:

$$\bar{\mathbf{n}}_l^t = \frac{\mathbf{Q}^{t-1} (\mathbf{Q}^0)^{-1} \mathbf{R} \bar{\mathbf{n}}_l^{t-1}}{1 + (\mathbf{t} - \mathbf{s}^0)^\top \mathbf{R} \bar{\mathbf{n}}_l^{t-1} + (\mathbf{s}^{t-1})^\top \mathbf{Q}^{t-1} (\mathbf{Q}^0)^{-1} \mathbf{R} \bar{\mathbf{n}}_l^{t-1}}. \quad (24)$$

Other homographies and view-normals can be corrected for ego-motion accordingly. The estimation of camera ego-motion of a stereo camera system is a well-studied problem

(e.g., [Badino and Kanade, 2011](#)). Here we use the method proposed in [Sec. 4.6](#).

#### 5.4 Approximate inference for view-consistency

Our inference procedure closely follows the approach for a single reference view in [Sec. 4.5](#). Again, we perform inference in a discrete CRF and optimize the energy in two steps, first solving for the mappings  $\mathcal{P}$ , while keeping the segmentation fixed. Then we proceed the other way around, fixing the mappings from segments to moving planes and optimizing w.r.t. to the segmentation mappings  $\mathcal{S}$ . The alternation can be iterated further, but again without practical benefits. Instead of an initial superpixel segmentation, we prefer to start from a regular checkerboard grid with an edge length of 16 pixels. Seed points  $\mathbf{e} \in \mathcal{E}$  (see [Eq. 20](#)) are simply the grid centers. This trivial “segmentation” is more efficient and also reduces aliasing artifacts, caused by a possibly uneven size of segments across views. The per-pixel refinement step ([Fig. 11](#)) will eventually deliver a consistent over-segmentation across views, adhering to depth and motion boundaries.

Because of the grid structure, segments can be treated as large pixels when solving for  $\mathcal{P}$ . However, the use of an initially not view-consistent segmentation will lead to aliasing effects. We thus relax the consistency constraints and set  $\varepsilon := 0.1$  and  $\theta_{\text{mvp}} := 3/16 \theta_{\text{oob}}$  in the first optimization round, to ensure that proposals are not discarded at an early stage. We generate the proposal set in the same manner as described in [Sec. 4.6](#). We discovered that by first running a single segment-to-plane step of our reference-view version above, and removing unused proposals, the proposal set is filtered without losing important information, leading to a significantly reduced computation time. When optimizing over more than two frames, proposals are generated for all consecutive frame pairs. *I.e.*, when using 3 frames we generate proposals for time steps  $t=-1$  and  $t=0$ , and additionally for  $t=1$  when using 4 frames. The additional proposals are discarded when they are found to be similar to already existing ones nearby. We consider proposals to be valid in a certain expansion region, centered at the seed point in the canonical frame. Empirically, we found that an expansion region size of  $13 \times 9$  cells ( $208 \times 144$  pixels) yields a good compromise between accuracy and speed. During a fusion

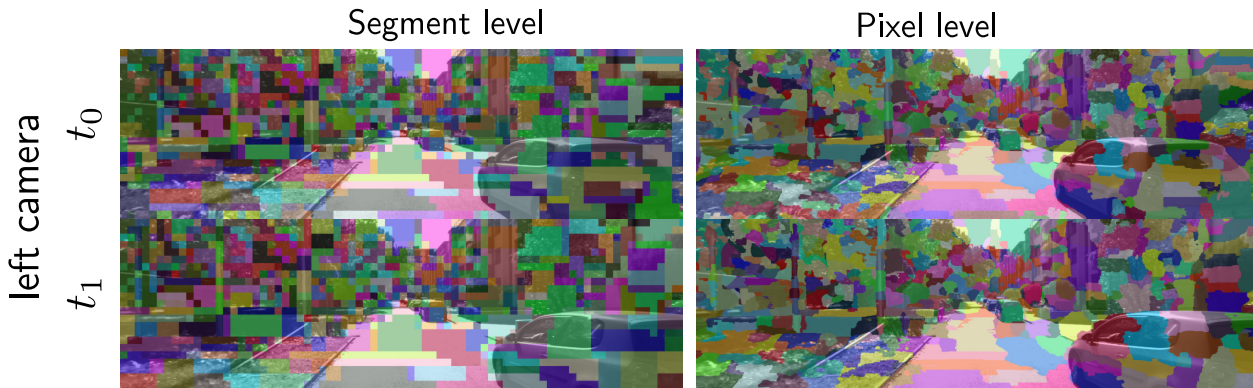


**Fig. 11** Example from the KITTI training set (#191): Consistent moving plane assignments at segment level (*left*) and final consistent superpixel segmentation (*right*).

move, we thus only have to instantiate a local graph, which is determined by a projection of the expansion region into all other views.

The inference for the pixel-to-segment mappings  $\mathcal{S}$  follows similar principles. Unused moving plane proposals are discarded. The size of the instantiated graph is restricted by the region constraint (Eq. 20), using an expansion region of  $39 \times 39$  pixels ( $N_S = 20$ ), and determined by projection into the other views. We penalize inconsistencies more strictly here, since the decisions are made on a per-pixel basis, and use the default parameters for  $\epsilon$  and  $\theta_{\text{mvp}}$  from Sec. 5.2. Fig. 11 illustrates the computed mappings over the course of the optimization for one of the cameras. Consistent moving plane assignments at segment level are shown on the left, illustrating the distribution of  $\mathcal{P}$ . The final, consistent superpixel segmentation  $\mathcal{S}$  is depicted on the right.

#### 5.4.1 Hierarchical refinement

The grid-based segment structure, furthermore, allows for a very simple refinement procedure, which we found to work well in practice. Instead of directly redistributing pixels to segments by solving for  $\mathcal{S}$  after all segments have been assigned a moving plane, we optionally refine the segmentation and solve for  $\mathcal{S}$  again. In practice we halve the grid resolution in each image and start the inference from the previous assignment. We prune the initial proposal set by retaining only those moving planes that are in use. In our experience, this hierarchical approach allows to reduce aliasing problems due to the smaller segment size, but still considers a more global context during the optimisation stage. Because we again set the expansion region to  $13 \times 9$  cells and the set of moving plane proposals is already reduced significantly, this step is very efficient. Note that after the refinement, we also reduce the expansion region (*i.e.*  $N_S = 10$ ) accordingly when re-assigning pixels to segments.

## 6 Experiments

We begin the experimental evaluation with our basic model based on a single reference view and later examine the view-consistent approach. Quantitative experiments rely on the KITTI dataset (Geiger et al, 2012), which has emerged as a standard benchmark for optical flow and stereo algorithms, with over 50 submissions in both categories. Its images are acquired by a calibrated stereo rig, mounted on top of a car together with a laser scanner, which delivers the semi-dense ground truth. Targeting automotive applications, the scenes are challenging for mainly two reasons. First, the strong forward motion of the car leads to very large displacements in stereo ( $> 150$  pixels) and flow ( $> 250$  pixels). Consequently, there are also many pixels without direct correspondence in the other image. Second, the images are acquired outdoors under realistic lighting conditions and exhibit over-saturation, shadows and lens flare, but also translucent and specular glass and metal surfaces. The KITTI benchmark is the first large scale dataset that allows evaluating scene flow methods along with their 2D counterparts, stereo and opti-

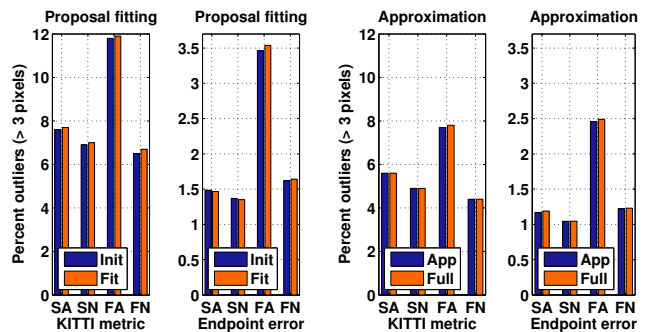


**Fig. 12** (*left*) Proposal fitting procedure: Error of the 2D proposal algorithms (blue) and after planar rigid segment fitting (orange). (*right*) Approximation of the regularization term after the per-segment step: Error when evaluating the integral per pixel (orange) and when integrating the distances at the endpoints of the shared edge (blue).

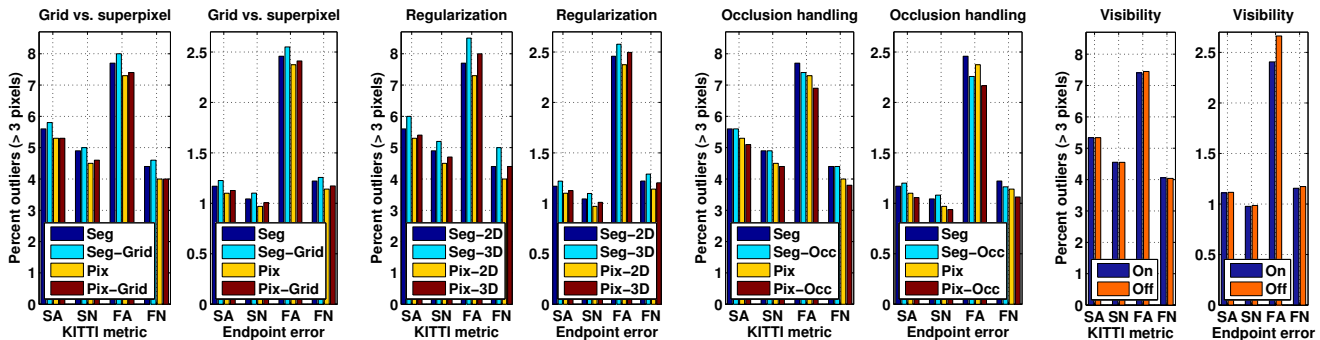


**Fig. 13** Evaluation of different model choices on the KITTI training set for the per-segment and the final solution after per-pixel refinement. (*left*) Initial segmentation: Using a grid (light blue and red) compared to a superpixel segmentation (blue and yellow). (*center left*) Regularization: Comparison of 2D (blue and yellow) and 3D regularization (light blue and red). (*center right*) Occlusion handling: Our basic model with (light blue and red) and without (blue and yellow) occlusion handling. (*right*) Visibility term: Predicting all pixels to stay in bounds (orange) compared to our standard predictor (blue) (only per-pixel error).

cal flow. However, it often lacks ground truth for independently moving objects, which leads to a bias toward methods that focus on the dominant background. Nonetheless, we strongly believe that this dataset is better suited for the evaluation of scene flow methods than other existing, synthetic datasets used previously (*e.g.*, [Huguet and Devernay, 2007](#); [Vogel et al, 2011](#)).

Our quantitative experiments mainly employ the KITTI training dataset, which is ideal for a detailed performance and parameter study due to its size of 194 images ( $1240 \times 376$  pixels) with public ground truth. For a comparison to the state of the art, we also submitted our results on the 195 images of the test portion of the KITTI dataset to the official KITTI benchmark (Sec. 6.5); there the ground truth is withheld. Because of inaccuracies in the laser measurements from the moving platform, the standard KITTI metric is to compute the number of outlier pixels that deviate more than a certain threshold from the ground truth. We report results for error thresholds of 2, 3, 4, and 5 pixels for the entire image (*All*), or only for unoccluded areas (*Noc*). We additionally report the endpoint error (*EPE*) for optical flow and stereo. We occasionally use the abbreviations *SN* for stereo without occluded areas, and *SA* when including these regions. Similarly, we shorten the respective identifiers for optical flow as *FN* and *FA*.

### 6.1 Evaluation of the single reference view model

All experiments use fixed parameters, except where stated. We set the smoothness weight to  $\lambda = 1/16$ , and the weight of the segmentation term relative to  $\lambda$  as  $\mu = 1/10\lambda$ . If not mentioned otherwise, we regularize in 2D space and fix  $\eta_G = \eta_M = 20$ .

We generate the proposal set from the output of 2D optical flow and stereo algorithms. For computing optical flow we employ the algorithm of [Vogel et al \(2013a\)](#), which uses

a census data term and a total generalized variation regularizer, a popular and effective combination for the KITTI scenes. To obtain an estimate in a reasonable time, we only apply 3 warps and 10 iterations per warp with an up-scaling factor of 0.9 in the image pyramid. The disparity map is obtained using semi-global matching ([Hirschmüller, 2008](#)).

First, we evaluate the proposal fitting procedure from Sec. 4.6. Fig. 12 (left) shows the KITTI metric at the default threshold (3 pixels), as well as the endpoint error of the plain 2D proposal algorithms (*Init*), and after the per-segment fitting took place (*Fit*). We observe only small changes in error, thus can conclude that planar rigid segment fitting does not significantly affect the accuracy. We attribute slight deviations in error to non-planar or non-rigid segments, *e.g.* due to misalignment with depth and motion boundaries.

Next, we investigate the simplification of the smoothness term when reasoning over segments, and how it affects the results. Recall that for computational efficiency we evaluate the spatial regularizer directly on the endpoint distances of the shared edge, instead of accumulating the contribution of all boundary pixels (Sec. 4.2). As we can see in Fig. 12 (right), the approximation (*App*) is quite accurate given our compact superpixels and on par with the exhaustive computation (*Full*), but in our experience  $\sim 30\times$  faster. Note that we here report results directly after the segment-level optimization, since both approaches employ the same per-pixel refinement step.

We now demonstrate that our representation and optimization approach are quite robust, in the sense that the results do not strongly depend on the initialization, parameter choice, *etc.* The importance of the initial segmentation is evaluated in Fig. 13 (left). Starting from a trivial “grid” segmentation (edge length 16 pixels) leads to a slight decrease in performance before the per-pixel refinement takes place. This gap is closed after the refinement step. Only a small difference in accuracy remains compared to starting

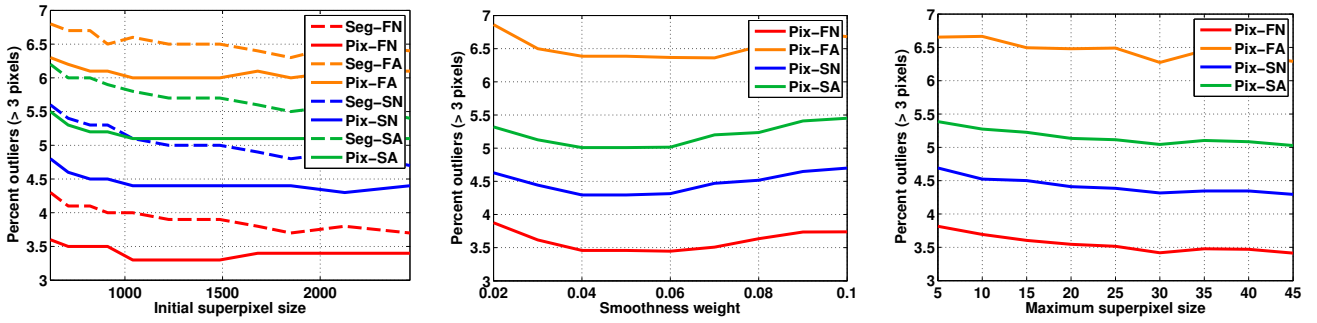


**Fig. 14** (left) Performance w.r.t. the number of initial superpixels. (center) Performance w.r.t. the smoothness weight  $\lambda$ . (right) Performance w.r.t. the maximum superpixel size  $N_S$ . The legend distinguishes *Pix(el)/Seg(ment)-F(low)/S(tereo)-A(l)/N(oc)*.

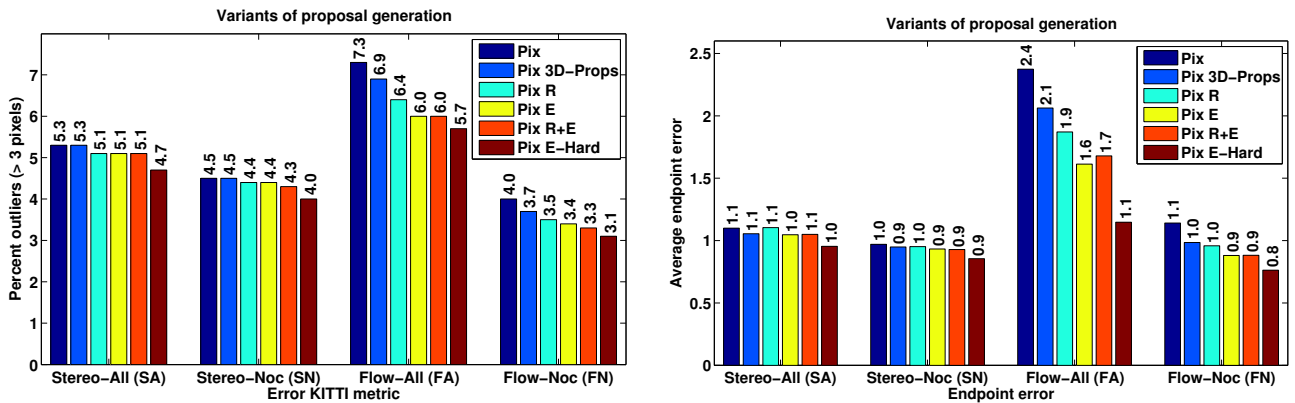


**Fig. 15** Comparison of different strategies to generate proposals: We compare using only 2D proposals (*Pix*), adding more proposals from scene flow algorithms (*3D-Props*), local replacement (*R*), ego-motion (*E*), a combination of both (*R+E*), and removing all but ego-motion proposals (*E-Hard (constraint)*). Errors are evaluated using the KITTI metric and w.r.t. the endpoint error after per-pixel refinement.

from a proper superpixel segmentation. Note that this also helps understanding why, as mentioned, iterating the alternating inference further has little practical benefit; energy and error are not significantly reduced further.

The effect of starting with a different number of superpixels is depicted on the left of Fig. 14. After using more than  $\sim 1000$  initial segments, the accuracy of the final result becomes stable, as the per-pixel refinement can compensate for eventual inaccuracies in the coarser initial segmentation. But even starting with fewer segments does not harm the performance dramatically.

Similarly, varying the weight for the regularization term  $\lambda$  (Fig. 14, center) and the maximum superpixel size  $N_S$  in the per-pixel refinement (Fig. 14, right) shows that the method is not sensitive to changes in these parameters. In the latter case higher values lead to better results, but also longer computation times.

Next, we investigate the behavior when switching from 2D to 3D regularization. For 3D regularization we set  $\eta_G = \eta_M = 5$  and  $\lambda = 0.25$ , thus increase the robustness in the smoothing process. We can observe from Fig. 13 (center left) that regularization w.r.t. 2D entities is slightly superior in the evaluated measures. This can possibly be explained by

the fact that the error measures do not evaluate the 3D quality of the scene flow, but only its reprojection, *i.e.* disparity and 2D optical flow.

Fig. 13 (right) depicts the effect of replacing the visibility prediction (Sec. 4.4) by a trivial predictor, which assumes pixels to always stay in bounds. As we can see, predicting visibility by the initial 2D algorithms has a strong effect on the flow endpoint error in occluded regions. Other measures, however, are nearly unaffected.

The biggest impact on the quality of the estimated scene flow is given by the different proposal algorithms we utilize. In Fig. 15 we extend our standard 2D proposal set by adding proposals from 3D scene flow methods (*3D-Props*), namely  $L_1$ -regularized 3D scene flow (Basha et al, 2010) and locally rigid 3D scene flow (Vogel et al, 2011). Furthermore, we evaluate our local replacement strategy (*R*), the ego-motion proposals (*E*, Sec. 4.6.1), and combine both proposal methods (*R+E*). Additionally, we evaluate a variant in which we replace the rigid motion component of our proposals with the estimated camera motion (*E-Hard*), thus simulating a motion stereo algorithm, which enforces a rigid scene with only ego-motion, similar to Yamaguchi et al (2013, 2014). We can observe that adding more proposals improves re-

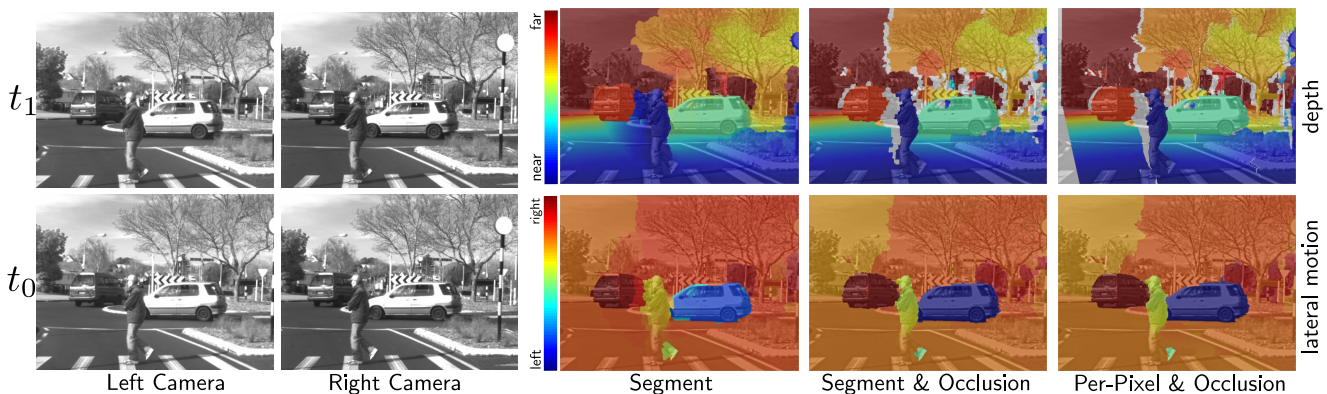


**Fig. 16** Example scene from Vaudrey et al (2008), demonstrating occlusion handling and the different processing steps. Results are given for the estimated depth and the lateral 3D motion component. Detected occlusions are highlighted in white.

sults; especially the endpoint error of optical flow is reduced. A larger gain is achieved by local replacement and, furthermore, by adding additional ego-motion proposals. Both approaches are complementary to some extent, as a combination slightly improves the results further. Finally, the best results can be achieved by enforcing ego-motion as a hard constraint, underlining the bias in the KITTI benchmark.

### 6.1.1 Evaluation of the occlusion model

We begin the evaluation of our occlusion model of Sec. 4.7 with a qualitative example of a street scene<sup>3</sup> from Vaudrey et al (2008). The scene is recorded from a vehicle approaching a roundabout. Several independently moving traffic participants and a rather complex occlusion pattern pose a challenging scenario for our method. Fig. 16 displays the results after the different processing steps of our approach. The estimate appears acceptable without occlusion handling, except for regions that are not visible in the reference image, e.g. at the left of the pedestrian. Adding the occlusion handling from Sec. 4.7 allows to detect occluded regions and to extrapolate the lateral motion in a plausible way. The per-pixel refinement (*Per-Pixel & Occlusion*) enhances the object contours and improves the occlusion boundaries even more.

We now quantitatively compare our basic model with and without additional occlusion handling. Fig. 13 (center right) shows a small, but consistent advantage of explicit occlusion handling. The gap is largest for optical flow evaluated over the whole image. Note, however, that with additional proposals the advantage diminishes and the difference between both models becomes smaller. Recall that in order

<sup>3</sup> Compared to KITTI images, the less challenging lighting conditions allow us to refrain from our usual census data cost. We use brightness constancy with  $\rho(a, b) = \min(|a - b|, \zeta)$ , truncated at  $\zeta = 10\%$  of the intensity range. We use 3D regularization with rather aggressive truncation parameters ( $\eta_G = \eta_M = 1$ ). Other deviating parameters were set to  $\lambda = 0.1, \mu = 0.1, \theta_{occ} = 0.03$ .

**Table 1** Optimization with explicit occlusion handling: Percentages of supermodular edges and resulting unlabeled nodes, resulting energy when using QPBO or QPBO-I. Numbers are averaged over the KITTI training set.

inference stage	supermodular edges	unlabeled nodes	energy w/ QPBO	energy w/ QPBO-I
Seg	4.8%	3.8%	760692	753196
Pix	1.3%	7.7%	678110	664497

to perform optimization with graph-cut based techniques, like QPBO, the higher-order potentials, which can occur in case of multiple occlusions, have to be reduced to pairwise ones (Sec. 4.7). The resulting optimization problem possesses supermodular edges, such that nodes can remain unlabeled after running QPBO. To approximately minimize this NP-hard problem, Rother et al (2007) proposed the QPBO-I method, which we also apply here. Table 1 summarizes our experience when applying the method on the KITTI training dataset. While the number of supermodular edges and unlabeled nodes appears to be small, employing QPBO-I instead of QPBO has a notable impact on the resulting energies. At the pixel level, the number of nodes that cannot be labeled by QPBO alone appears rather high at 7.7%. Optimization with QPBO-I, however, takes an order of magnitude more time. Another challenge is that this form of occlusion reasoning is sensitive to outliers in the data term, such as specular highlights on the window of the car in Fig. 16. Note that without occlusion handling unlabeled nodes occur only very rarely ( $< 1$  per image).

## 6.2 Evaluation of the view-consistent model

As before, we keep all parameters fixed, unless otherwise mentioned. The only parameter that deviates strongly from the reference-view model is the smoothness weight. We set  $\lambda = 1/60$ , and regularize using the intensity-weighted edge length (Eq. 13), which is now based on multiple images. We

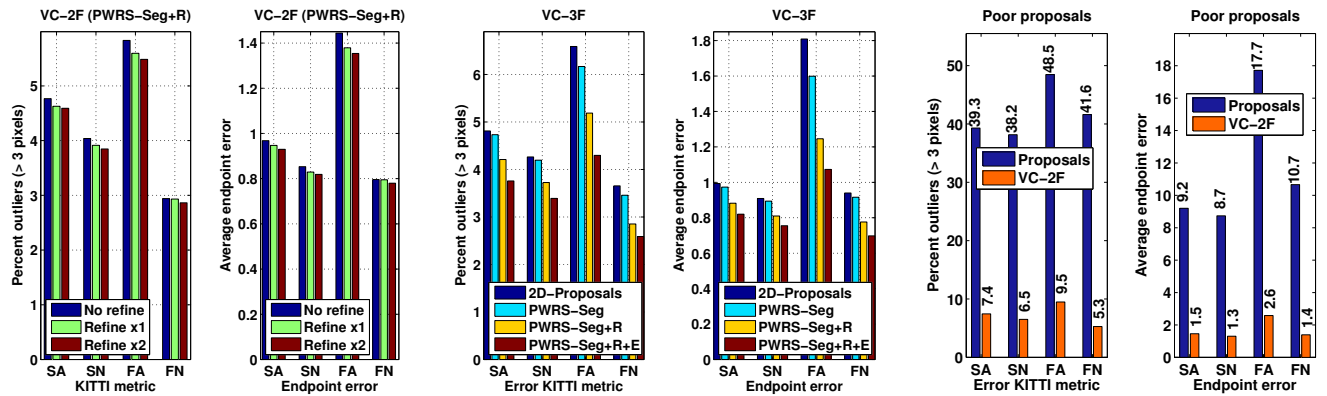


Fig. 17 (left) Error after refining the segmentation in the two-frame model, once (green), twice (red), or not at all (blue). (center) Effect of the proposals on the view-consistent three-frame model: 2D proposals (blue), single reference-view model (light blue), local replacement (yellow), and additional ego-motion (red). (right) Evaluation with a poor proposal set: 2D proposals (blue) and VC-2F (orange), with PWRS-Seg+R pruning. Results are shown w.r.t. the KITTI metric ( $> 3$  pixels) and the endpoint error.

set  $N_S = 20$  to speed up the per-pixel refinement, and start from an initial grid segmentation.

We begin with several quantitative analyses to illustrate the different aspects of the proposed approach. First, we investigate whether our model can benefit from the hierarchical refinement of the grid described in Sec. 5.4.1. Fig. 17 (left) compares the performance after a single and two refinement levels to the result without hierarchical refinement. The gain in performance is not large, but consistent throughout the evaluation; we use a single refinement step in the remaining experiments.

As our model is capable of jointly reasoning over multiple frames by assuming constant velocity for the rigidly moving segments, we investigate the performance when considering 2, 3, or 4 consecutive frames in Fig. 18. We further distinguish the addition of proposals from time steps other than the current one (“+”), meaning that we derive proposals from the disparity and 2D flow computed from the other adjacent frame pairs in the time window. Moreover, we include a variant that reasons about only two frames, but is provided with proposals extracted from three frames ( $VC-2F+$ ). For comparison, we also add the single reference-view version  $PWRS+R$  (with local replacement), which is used to reduce the initial proposal set of the current frame pair. Note again that this reference-view method is only applied at the segment level.

Analyzing Fig. 18 one can observe that moving away from the single reference view ( $PWRS+R$  vs.  $VC-2F$ ) already yields a significant improvement, most notably in the optical flow error w.r.t. all pixels. View-consistency benefits by considering the data of all views jointly. Parts that are occluded in the canonical view used for evaluation (and as a reference view  $PWRS+R$ ) can still be visible in two other views. Furthermore, a strong drop in the endpoint error hints at a reduction of gross outliers. Including proposals from

the previous time step ( $VC-2F+$ ), and considering the image data of the previous frames ( $VC-3F$ ) improve the results further. But only a combination ( $VC-3F+$ ) of both leads to a larger performance gain in all measures, again affecting occluded regions most strongly. This suggests that a larger set of proposals from multiple frames alone is not sufficient, but that the image evidence from the longer sequence is important. Finally, including a fourth frame into the model yields diminishing returns, with only marginal improvements over the three frame case.

In another experiment we analyze the effect of the proposal set. Recall that we use the reference-view version of our method in order to prune the proposal set in the beginning, with the advantage of a reduced computation time for the view-consistent model. Fig. 17 (center), however, also shows an effect on the accuracy of the algorithm, here evaluated for the three frame case without considering additional proposals from the previous time step. Interestingly, despite the fact that the application of  $PWRS-Seg$  yields only a subset of the original proposals ( $2D-Proposals$ ), the results improve. An analysis shows that both variants deliver almost the same final energy, such that the cause is not well-captured by our energy formulation. We posit that this may be due to the proposal set not being sufficiently varied in crucial parts of the solution space, which is supported by the fact that the observed accuracy difference diminishes when we use proposals from the previous time step as well ( $VC-3F+$ ). As we would expect given previous results (Fig. 15), we observe a strong gain in accuracy from the local replacement strategy ( $PWRS-Seg+R$ ) and ego-motion proposals ( $PWRS-Seg+R+E$ ); in these cases the additional proposals also noticeably lower the final energy.

Because our method requires proposals for computing scene flow, we investigated how much a poor proposal set affects the performance. To that end we change the param-

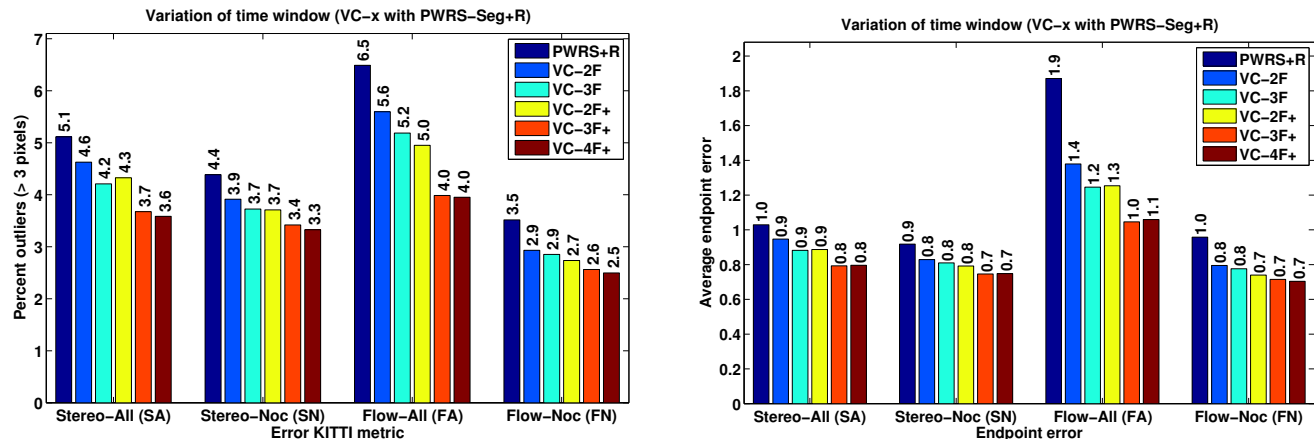


**Fig. 18** Evaluation across different number of frames: Single reference-view method on 2 frames (dark blue), view-consistent method on 2 frames (blue), 3 frames (cyan), 2 frames with proposals from the previous frame (yellow), 3 frames with proposals from previous frame (orange), and 4 frames with proposals from all 4 frames (red). Results are shown w.r.t. the KITTI metric ( $> 3$  pixels) and the endpoint error.

**Table 2** Optimization in the view-consistent model (3 frames): Average number of nodes and edges in the graph, average percentage of supermodular edges and resulting unlabeled nodes (before applying QPBO-I), and resulting energy when using LSA-AUX or QPBO-I. Numbers are averaged over the KITTI training set.

inference stage	# nodes	# edges	super-modular	unlabeled	energy QPBO-I	energy LSA-AUX
Seg	2064	7485	4.01%	0.4%	3295790	3306453
Pix	3749	20102	0.64%	1.2%	2907666	2908031

eters of the initial 2D stereo and flow algorithms. For instance, in the optical flow case we use only a single warp per image pyramid and change the pyramid scale to 0.5. We then apply our two-frame view-consistent method ( $VC-2F$ ) with  $PWRS-Seg+R$  to reduce the proposal set. The result is depicted in Fig. 17 (right). The notably high error of the 2D algorithms is reduced by a factor of 6 on average, showing that our scene flow approach can also cope with unfavorable proposal sets. This somewhat surprising result, achieved without considering ego-motion information, can partially be explained by the particularities of the dataset and the algorithms used to compute the proposals. The flow algorithm should deliver reasonable results in areas with only small 2D motion vectors. Given the largely planar nature of the street scenes in the dataset, these parts can then be propagated into other image areas, which have the same 3D motion and geometry, but strongly differing 2D motion. This in turn suggests that 3D scene flow may be well-suited to cope with large motions due to its internal 3D representation.

Recall that the formulation of the data term, although directly leading to only pairwise edge potentials, introduces supermodular edges into the energy. In Table 2 we investigate the situation in a similar manner as for the occlusion handling strategy with a single reference view, again collecting data over the whole KITTI training set. We apply the

QPBO-I algorithm to the optimization problem given by our three-frame version ( $VC-3F$ ) and count the number of unlabeled nodes and supermodular edges over the course of the optimization. As we can see, the number of non-submodular edges is not much lower than in the reference-view case, but unlabeled nodes occur significantly less often. This motivates us to also consider a different but more efficient graph construction<sup>4</sup>: The LSA-AUX algorithm (Gorelick et al., 2014) is applied at each expansion step, in order to find a submodular approximation of the problem. Conveniently, the local approximation bounds the true energy from above, such that the overall energy cannot increase, which is not the case if supermodular terms are just truncated. The final solutions show a comparable energy to results obtained with QPBO-I, while being an order of magnitude faster. Instead of LSA-AUX a similar performance can be also obtained by using QPBO without improve moves, where the former method delivers a moderate (10 – 15%) speed-up.

### 6.3 Qualitative examples

We begin with an illustration of several difficult examples from the KITTI benchmark (Fig. 19) recovered by our three-frame method ( $VC-3F+$ ). The most interesting example is shown at the top (#74). In the presence of severe lens flares in both cameras, many optical and scene flow methods fail hopelessly to recover the motion in this scene. While the appearance of these artifacts is rather consistent in consecutive views, their location is not. This allows our approach to recover the scene flow reasonably well. Notably only 8.1% of the flow vectors of all pixels and 5.7% in the visible areas are outside the standard 3-pixel error threshold of KITTI. It

<sup>4</sup> compared to QPBO the graph contains only half of the nodes

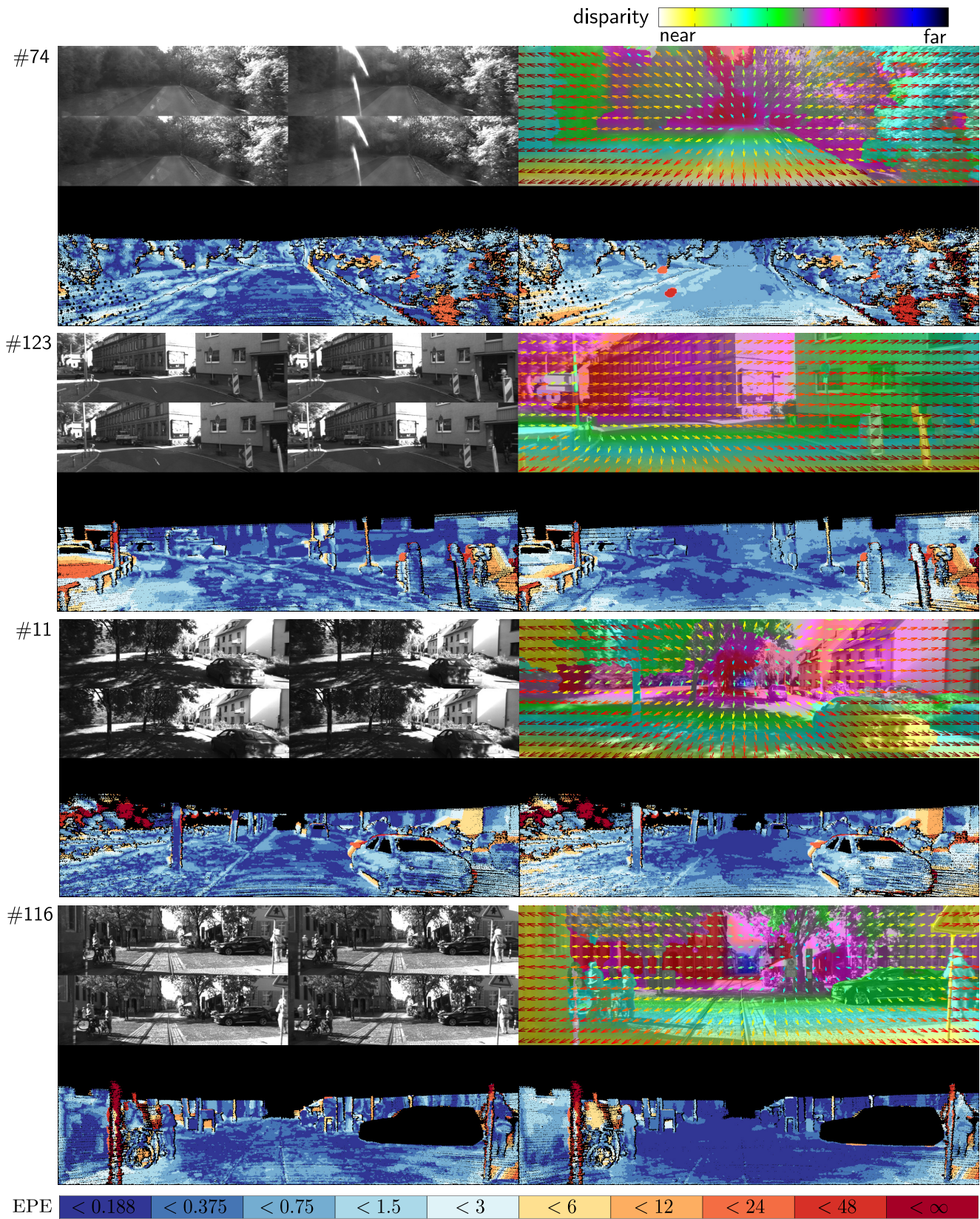


**Fig. 19** Examples from the KITTI training set. Input images (*top left*) and recovered scene flow (*top right*), color coded as disparity (from white – near to blue – far) and motion vectors, reprojected into the image plane. Arrow lengths are depicted with a log-scale. Colors encode the length of the actual 2D displacement (blue – small to red – large). Color coded endpoint error for disparity (*bottom left*) and flow (*bottom right*).

is important to note that the robust handling of these artifacts is achieved only through view- and multi-frame consistency. Also depicted is a scene (#11) with low image contrast in shadow regions. Scene #123 is interesting because of similar problems with lens flare as for #74, here however challenging the reconstruction of the geometry as their location is consistent across frames. Finally #116 has fine structures in the image (e.g., the traffic sign), several areas with occlusions, and a car moving independently, albeit without ground truth.

Fig. 20 illustrates results for different outdoor scenes from Meister et al (2012). We display the input images on the left. Our scene flow estimates (*VC-3F+*) are shown as disparities (center) and reprojected optical flow in the usual color coding. These examples show that our model is capable of handling independent object motion under unfavorable conditions. Even though the motion displacements in the image plane are rather small, the scenes contain many scenarios that are hard for conventional flow and stereo algorithms. The scenes ‘car truck’ and ‘crossing’ have saturated highlights and reflections, as well as a rather complex occlusion pattern. The scene ‘car truck’ also exhibits cast shadows dancing on the truck and the street. More challenging is ‘sun flares’, where the sun causes lens flares and ‘flying snow’, which as the name suggests contains heavy snow fall and a wet and reflecting street. The scene from Fig. 2 shows the wiper occluding the view and is, therefore, very difficult to recover for conventional approaches that parameterize the scene in a single camera only. The most complex scene is ‘night snow’, in which the aperture of the cameras is wide open and the image has only a shallow depth of field. Moreover, the windshield is wet, causing the headlights of approaching cars to flare. We can only give a qualitative evaluation here, as no ground truth for these scenes is available. Apart from the last scene, which has an incorrect depth in the sky region, our estimates appear quite appropriate.

### 6.3.1 Typical failure cases

Fig. 21 displays some typical failure cases of our method. For example, it is challenged by over-saturated areas, especially if these are located close to the boundary of the images or in occlusion regions. Recall that we replace the data term with a fixed penalty ( $\theta_{occ}$  or  $\theta_{ob}$ ), if a pixel lacks a correspondence in other images. Now assume that a proposal exists that maps this over-saturated image region to a similarly over-saturated, but incorrect one in the other images. The data penalty in this case is close to zero, which compared to the energy of the true solution in our model ( $\theta_{ob}$ ) is decidedly lower. By demanding view-consistency, this incorrect solution will still incur penalties for the incorrect regions, since the geometry and/or motion is not consistent. However, as the penalties are accumulated per pixel, whether the

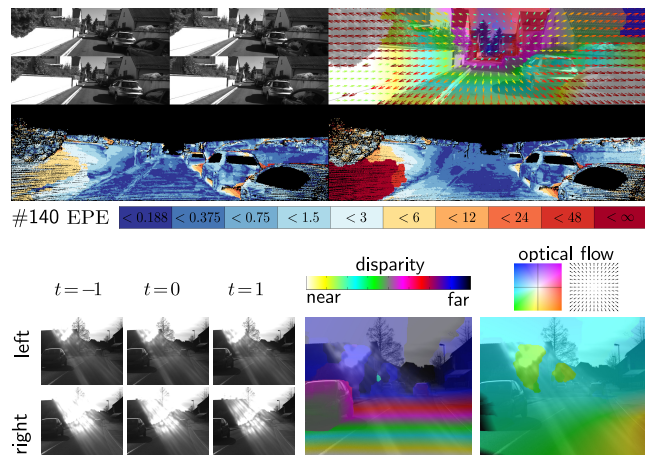


**Fig. 21** Typical failure cases from the KITTI training set: (top) Over-saturated area moving out of viewing frustum at the wall on the left. (bottom) Example from Meister et al (2012) showing a sun flare with a consistent motion pattern.

correct correspondence can be recovered depends on the size of the respective regions in the images.

As already mentioned, a second challenge are imaging artifacts, e.g. sun flares (Fig. 21, bottom), that appear consistently in all the views. In the example the sun flare even leads to over-saturation, such that the low data energy may overrule the consistency penalty.

## 6.4 Quantitative summary and timings

A direct comparison between the view-consistent and single reference-view models is given in Table 3. Note that these differ from the published results in (Vogel et al, 2013b, 2014) due to a change in the KITTI ground truth, slightly different parameter sets, and extensions such as the local replacement strategy. The first row gives results for the 2D algorithms used to derive the proposals (*2D Algorithms*). Otherwise, we use the usual notation: *PWRS* for our basic reference-view model, *PWRS+R* for a version with local replacements, and *PWRS+R+E* to denote the usage of additional ego-motion proposals. For the view-consistent version (*VC*) we use *PWRS+R+E* to prune the proposals and distinguish between the two, three and four-frame versions, with (+) and without proposals from all frames. In general the numbers improve from top to bottom. Already our basic version achieves a significant reduction in all error measures compared to the state-of-the-art 2D proposals. Both strategies to generate additional proposals show their benefit, especially for flow. The view-consistent model leads to a visible reduction of the error in all measures already for the two-frame case. Moving to three frames further improves the results, especially for occluded areas, but considering four frames only yields marginal improvements. Notably,

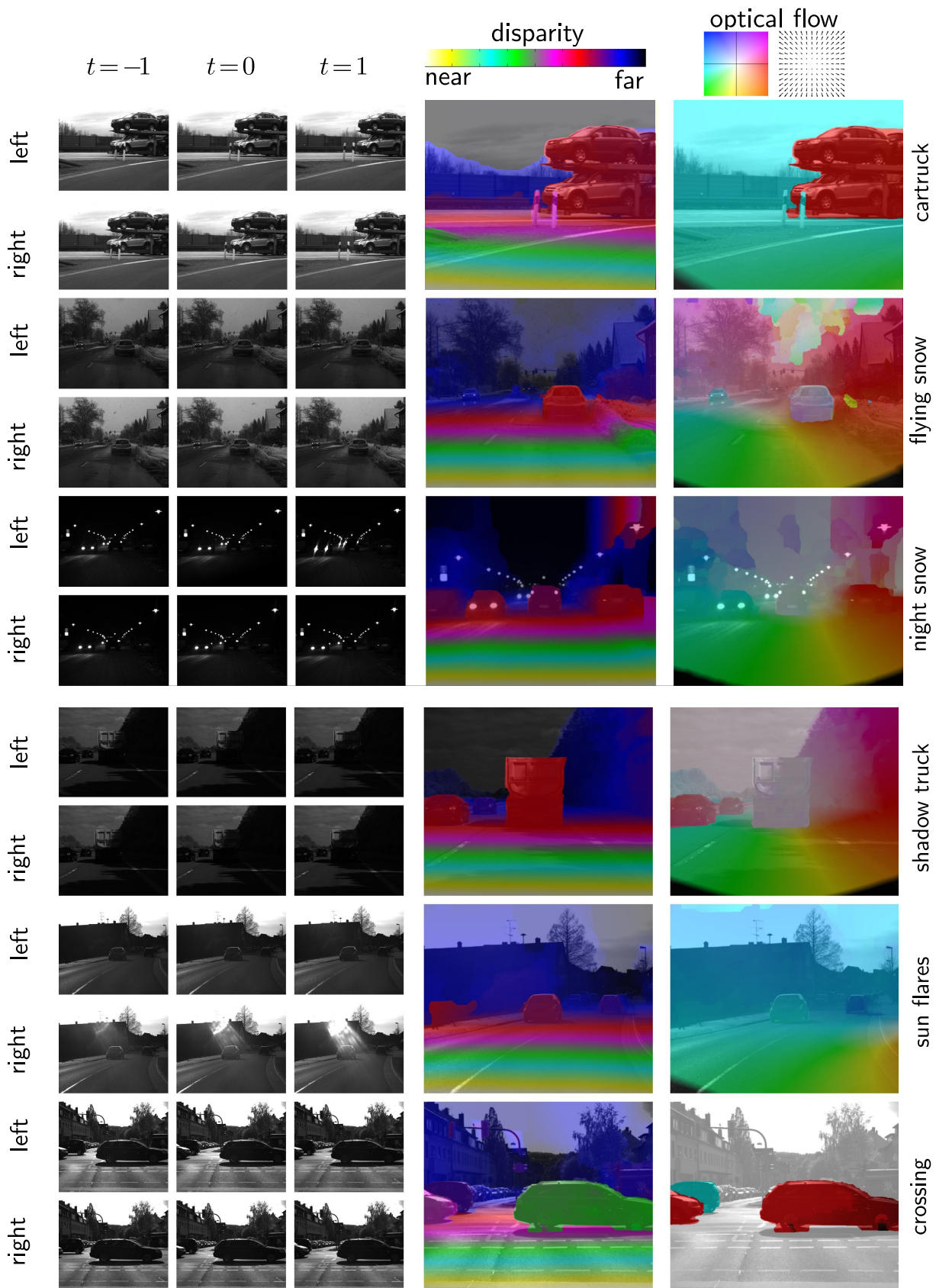


Fig. 20 Challenging examples from Meister et al (2012): Input frames of our method (*left*). Recovered scene flow, reprojected to disparity (*center*) and 2D flow field (*right*).

**Table 3** Results on the *KITTI training set*: Average KITTI metric (% of flow vectors / disparities above 2, 3, 4, 5 pixels of endpoint error) and average endpoint error [px] with (All) and without (Noc) counting occluded regions.

Method	Flow										Stereo									
	KITTI metric								AEP		KITTI metric								AEP	
	All				Noc				All	Noc	All				Noc				All	Noc
	2px	3px	4px	5px	2px	3px	4px	5px			2px	3px	4px	5px	2px	3px	4px	5px		
2D Algorithms	14.6	11.7	10.1	9.0	8.5	6.5	5.5	4.8	3.5	1.6	10.3	7.5	6.1	5.2	9.4	6.8	5.5	4.7	1.5	1.4
PRSF	9.9	7.3	6.0	5.2	5.7	4.0	3.2	2.7	2.4	1.1	7.7	5.3	4.1	3.4	6.7	4.5	3.5	2.9	1.1	1.0
PRSF+R	9.1	6.4	5.0	4.3	5.2	3.5	2.7	2.3	1.9	1.0	7.4	5.1	4.0	3.3	6.4	4.4	3.4	2.9	1.1	1.0
PRSF+R+E	8.6	6.0	4.7	3.9	5.0	3.3	2.6	2.1	1.7	0.9	7.3	5.1	4.0	3.3	6.3	4.3	3.4	2.8	1.0	0.9
VC-2F	7.8	5.2	4.0	3.2	4.3	2.8	2.1	1.7	1.2	<b>0.7</b>	6.6	4.5	3.5	2.8	5.7	3.8	2.9	2.4	0.9	0.8
VC-2F+	7.4	4.9	3.7	3.0	4.2	2.7	2.0	1.7	1.2	<b>0.7</b>	6.2	4.2	3.3	2.7	5.4	3.6	2.8	2.3	0.9	0.8
VC-3F	6.9	4.3	3.1	2.5	4.1	2.6	1.9	1.6	<b>1.1</b>	<b>0.7</b>	5.7	3.8	2.9	2.3	5.1	3.4	2.6	<b>2.1</b>	<b>0.8</b>	0.8
VC-3F+	6.4	4.0	<b>2.8</b>	<b>2.2</b>	4.0	<b>2.5</b>	1.9	<b>1.5</b>	<b>1.1</b>	<b>0.7</b>	5.4	<b>3.6</b>	<b>2.8</b>	2.3	5.0	3.4	2.6	<b>2.1</b>	<b>0.8</b>	<b>0.7</b>
VC-4F+	<b>6.3</b>	<b>3.9</b>	<b>2.8</b>	<b>2.2</b>	<b>3.9</b>	<b>2.5</b>	<b>1.8</b>	<b>1.5</b>	<b>1.1</b>	<b>0.7</b>	<b>5.2</b>	<b>3.6</b>	<b>2.8</b>	<b>2.2</b>	<b>4.8</b>	<b>3.3</b>	<b>2.5</b>	<b>2.1</b>	<b>0.8</b>	<b>0.7</b>

**Table 4** Timings on KITTI images (0.5MPixels), measured on a dual *Intel Core i7* computer and two proposals per segment, for two different numbers of initial segments.

# Segments	Proposals		PWRS				VC-SF						
	Init	Fit	Seg	R	E	Pix	Seg-2F	Seg-Ref-2F	Seg-3F	Seg-Ref-3F	Pix-2F	Pix-3F	
1850	60s	16s	19s	8s	9s	15s	23s		9s	46s	12s	18s	30s
1150	60s	16s	10s	8s	5s	10s	17s		6s	32s	8s	14s	23s

all but two numbers are at least halved when comparing our best result with the initial 2D solution.

Table 4 illustrates the time spent on the different parts of the algorithm. We distinguish between running the 2D flow and stereo algorithms (*Init*), the proposal fitting procedure (*Fit*), and further time the inference at the segment level (*Seg*) and at the pixel level (*Pix*). We also show the time needed for generating additional proposals (*R* and *E*), and one hierarchical refinement step (*Ref*). We compare numbers when starting with 1850 and 1150 segments. In both cases, our model with a single reference view (*PWRS*) needs less time for the optimization and both additional proposal generation strategies than for computing the initial optical flow and disparity maps. For the view-consistent case, we exploit the reduction in the number of proposals by first running *PWRS+R+E* at the segment level. With a low number of segments, our basic version (*PWRS*) needs only 20s to deliver a result. However, running the 2D proposal algorithms already takes significantly more time. Our most advanced three-frame method needs  $\sim 3$  minutes including proposals.

## 6.5 Comparison with the state of the art

Table 5 shows a comparison of our piecewise rigid scene model with the state of the art on the KITTI test set. At the time of writing (August 2014), the benchmark has over 50 submissions in both categories. Our scene flow methods rank among the top performers, with the view-consistent

model coming out first overall for both stereo and flow, when considering full images with occluded areas. Note that several top-ranked methods assume epipolar motion as a hard constraint (Setting *ms*). In contrast, our method can handle scenes with independently moving objects (*c.f.* Fig. 20), which are uncommon in the benchmark. Considering only methods applicable to general scenes, *i.e.* with independent object motion, the distance to the next best competitor is rather large, which demonstrates that scene flow from our piecewise rigid scene model, has a clear advantage over single camera methods for motion estimation under challenging conditions.

## 7 Conclusion

In this paper we introduced a scene flow approach that models dynamic scenes as a collection of piecewise planar, local regions, moving rigidly over time. It allows to densely recover geometry, 3D motion, and an over-segmentation of the scene into moving planes, leading to accurate geometry and motion boundaries. Employing unified reasoning over geometry, motion, segmentation and occlusions within the observed scene, our method achieves leading performance in a popular benchmark, surpassing dedicated state-of-the-art stereo and optical flow techniques at their respective task. We extend our basic reference-view technique to leverage information from multiple consecutive frames of a stereo video. Our view-consistent approach exploits consistency

**Table 5** Comparison with the state-of-the-art on the *KITTI test set*: Our methods are denoted as PRSF+R (reference view, 2D proposals, local replacement), PRSF+R+E (with ego-motion proposals), and VC-3F+ (view consistent, 3 frames, using PRSF+R to reduce the proposal set). The settings column marks scene flow (sf), multi-frame (mv), and motion stereo (ms) methods.

Stereo evaluation						Optical flow evaluation					
Method	Setting	KITTI metric (% > 3 px)		EPE [px]		Method	Setting	KITTI metric (% > 3 px)		EPE [px]	
		All	Noc	All	Noc			All	Noc	All	Noc
(Yamaguchi et al, 2014)	sf ms	3.64	<b>2.83</b>	0.9	<b>0.8</b>	VC-3F+	sf mv	<b>4.84</b>	<b>2.72</b>	<b>1.3</b>	<b>0.8</b>
VC-3F+	sf mv	<b>3.31</b>	3.05	<b>0.8</b>	<b>0.8</b>	(Yamaguchi et al, 2014)	sf ms	5.61	2.82	<b>1.3</b>	<b>0.8</b>
(Yamaguchi et al, 2013)		4.72	3.40	1.0	<b>0.8</b>	PRSF+R+E	sf	7.07	3.57	1.6	0.9
(Yamaguchi et al, 2013)		5.11	3.92	1.0	0.9	(Yamaguchi et al, 2013)	ms	8.28	3.64	2.2	0.9
PRSF+R+E	sf	4.87	4.02	1.0	0.9	PRSF+R	sf	7.39	3.76	2.8	1.2
(Yamaguchi et al, 2012)		5.37	4.04	1.1	0.9	(Yamaguchi et al, 2013)	ms	10.56	3.91	2.7	0.9
PRSF+R	sf	5.22	4.36	1.1	0.9	(Ranftl et al, 2014)		11.96	5.93	3.8	1.6
(Einecke and Eggert, 2014)		5.94	4.86	1.2	1.0	(Braux-Zin et al, 2013)		15.15	6.20	4.5	1.5
(Spangenberg et al, 2013)		6.18	4.97	1.6	1.3	(Demetz et al, 2014)		11.03	6.52	2.8	1.5
(Ranftl et al, 2013)		6.88	5.02	1.6	1.0	(Vogel et al, 2013a)		14.57	7.11	5.5	1.9

over time and viewpoints, thereby significantly improving 3D scene flow estimation. In particular, our model shows remarkable robustness to missing evidence, outliers, and occlusions, and can recover motion and geometry even under unfavorable imaging conditions, where many methods fail.

In future work we plan to incorporate long-term temporal consistency into our framework, and to relax the constant velocity assumption to a more flexible formulation. Moreover, we aim to explicitly model small deviations from the local planarity and rigidity assumptions. Another promising route may be to include object-level semantic image understanding into the segmentation scheme, with associated class-specific motion and geometry models.

**Acknowledgements** SR was supported in part by the European Research Council under the European Union’s Seventh Framework Programme (FP/2007-2013) / ERC Grant Agreement No. 307942, as well as by the EU FP7 project “Harvest4D” (No. 323567).

## References

- Adiv G (1985) Determining three-dimensional motion and structure from optical flow generated by several moving objects. *IEEE Transactions on Pattern Analysis and Machine Intelligence* 7(4):384–401
- Ali AM, Farag AA, Gimel’Farb GL (2008) Optimizing binary MRFs with higher order cliques. In: *European Conference on Computer Vision*
- Badino H, Kanade T (2011) A head-wearable short-baseline stereo system for the simultaneous estimation of structure and motion. In: *IAPR Conference on Machine Vision Application*, pp 185–189
- Baker S, Scharstein D, Lewis J, Roth S, Black MJ, Szeliski R (2011) A database and evaluation methodology for optical flow. *International Journal of Computer Vision* 92(1):1–31, [vision.middlebury.edu/flow](http://vision.middlebury.edu/flow)
- Barnes C, Shechtman E, Finkelstein A, Goldman DB (2009) PatchMatch: A randomized correspondence algorithm for structural image editing. *ACM Transactions on Graphics* 28(3):24:1–24:11
- Basha T, Moses Y, Kiriyati N (2010) Multi-view scene flow estimation: A view centered variational approach. In: *IEEE Conference on Computer Vision and Pattern Recognition*

- Black MJ, Anandan P (1991) Robust dynamic motion estimation over time. In: *IEEE Conference on Computer Vision and Pattern Recognition*
- Black MJ, Jepson AD (1996) Estimating optical flow in segmented images using variable-order parametric models with local deformations. *IEEE Trans Pattern Anal Mach Intell* 18(10):972–986, DOI 10.1109/34.541407, URL <http://dx.doi.org/10.1109/34.541407>
- Bleyer M, Rother C, Kohli P (2010) Surface stereo with soft segmentation. In: *IEEE Conference on Computer Vision and Pattern Recognition*
- Bleyer M, Rhemann C, Rother C (2011a) PatchMatch stereo – Stereo matching with slanted support windows. In: *British Machine Vision Conference*
- Bleyer M, Rother C, Kohli P, Scharstein D, Sinha SN (2011b) Object stereo – Joint stereo matching and object segmentation. In: *IEEE Conference on Computer Vision and Pattern Recognition*
- Braux-Zin J, Dupont R, Bartoli A (2013) A general dense image matching framework combining direct and feature-based costs. In: *IEEE International Conference on Computer Vision*
- Brox T, Malik J (2011) Large displacement optical flow: Descriptor matching in variational motion estimation. *IEEE Transactions on Pattern Analysis and Machine Intelligence* 33(3):500–513
- Brox T, Bruhn A, Papenberg N, Weickert J (2004) High accuracy optical flow estimation based on a theory for warping. In: *European Conference on Computer Vision*
- Carceroni RL, Kutulakos KN (2002) Multi-view scene capture by surfel sampling: From video streams to non-rigid 3D motion, shape and reflectance. *International Journal of Computer Vision* 49:175–214
- Courchay J, Pons JP, Monasse P, Keriven R (2009) Dense and accurate spatio-temporal multi-view stereovision. In: *Asian Conference on Computer Vision*
- Demetz O, Stoll M, Volz S, Weickert J, Bruhn A (2014) Learning brightness transfer functions for the joint recovery of illumination changes and optical flow. In: *European Conference on Computer Vision*, to appear
- Devernay F, Mateus D, Guilbert M (2006) Multi-camera scene flow by tracking 3-D points and surfels. In: *IEEE Conference on Computer Vision and Pattern Recognition*
- Einecke N, Eggert J (2014) Block-matching stereo with relaxed fronto-parallel assumption. In: *Intelligent Vehicles*, pp 700–705
- Furukawa Y, Ponce J (2008) Dense 3D motion capture from synchronized video streams. In: *IEEE Conference on Computer Vision and Pattern Recognition*

- Garg R, Roussos A, Agapito L (2013) A variational approach to video registration with subspace constraints. *International Journal of Computer Vision* 104(3):286–314
- Geiger A, Lenz P, Urtasun R (2012) Are we ready for autonomous driving? In: *IEEE Conference on Computer Vision and Pattern Recognition*, [www.cvlibs.net/datasets/kitti/](http://www.cvlibs.net/datasets/kitti/)
- Gorelick L, Veksler O, Boykov Y, Ben Ayed I, DeLong A (2014) Local submodular approximations for binary pairwise energies. In: *Computer Vision and Pattern Recognition*
- Hirschmüller H (2008) Stereo processing by semiglobal matching and mutual information. *IEEE Transactions on Pattern Analysis and Machine Intelligence* 30(2):328–341
- Hornacek M, Fitzgibbon A, Rother C (2014) SphereFlow: 6 DoF scene flow from RGB-D pairs. In: *IEEE Conference on Computer Vision and Pattern Recognition*
- Huguet F, Devernay F (2007) A variational method for scene flow estimation from stereo sequences. In: *IEEE International Conference on Computer Vision*
- Hung CH, Xu L, Jia J (2013) Consistent binocular depth and scene flow with chained temporal profiles. *International Journal of Computer Vision* 102(1-3):271–292
- Irani M (2002) Multi-frame correspondence estimation using subspace constraints. *International Journal of Computer Vision* 48(3):173–194
- Ishikawa H (2009) Higher-order clique reduction in binary graph cut. In: *IEEE Conference on Computer Vision and Pattern Recognition*
- Ju S, Black M, Jepson A (1996) Skin and bones: multi-layer, locally affine, optical flow and regularization with transparency. In: *IEEE Conference on Computer Vision and Pattern Recognition*, pp 307–314, DOI 10.1109/CVPR.1996.517090, URL [http://ieeexplore.ieee.org/xpls/abs\\_all.jsp?arnumber=517090](http://ieeexplore.ieee.org/xpls/abs_all.jsp?arnumber=517090)
- Kolmogorov V, Zabih R (2001) Computing visual correspondence with occlusions using graph cuts. In: *IEEE International Conference on Computer Vision*, pp 508–515
- Lempitsky V, Roth S, Rother C (2008) FusionFlow: Discrete-continuous optimization for optical flow estimation. In: *IEEE Conference on Computer Vision and Pattern Recognition*
- Lempitsky V, Rother C, Roth S, Blake A (2010) Fusion moves for Markov random field optimization. *IEEE Transactions on Pattern Analysis and Machine Intelligence* 32(8):1392–1405
- Lucas BD, Kanade T (1981) An iterative image registration technique with an application to stereo vision. In: *International Joint Conference on Artificial Intelligence*, vol 2
- Meister S, Jähne B, Kondermann D (2012) Outdoor stereo camera system for the generation of real-world benchmark data sets. *Optical Engineering* 51(2)
- Müller T, Rannacher J, Rabe C, Franke U (2011) Feature- and depth-supported modified total variation optical flow for 3D motion field estimation in real scenes. In: *IEEE Conference on Computer Vision and Pattern Recognition*
- Murray DW, Buxton BF (1987) Scene segmentation from visual motion using global optimization. *IEEE Transactions on Pattern Analysis and Machine Intelligence* 9(2):220–228
- Nir T, Bruckstein A, Kimmel R (2008) Over-parameterized variational optical flow. *International Journal of Computer Vision* 76(2):205–216
- Park J, Oh TH, Jung J, Tai YW, Kweon IS (2012) A tensor voting approach for multi-view 3D scene flow estimation and refinement. In: *European Conference on Computer Vision*
- Rabe C, Müller T, Wedel A, Franke U (2010) Dense, robust, and accurate motion field estimation from stereo image sequences in real-time. In: *European Conference on Computer Vision*
- Ranftl R, Pock T, Bischof H (2013) Minimizing TGV-based variational models with non-convex data terms. In: *Scale Space and Variational Methods in Computer Vision*
- Ranftl R, Bredies K, Pock T (2014) Non-local total generalized variation for optical flow estimation. In: *European Conference on Computer Vision*, to appear
- Rother C, Kolmogorov V, Lempitsky V, Szummer M (2007) Optimizing binary MRFs via extended roof duality. In: *IEEE Conference on Computer Vision and Pattern Recognition*
- Rother C, Kohli P, Feng W, Jia J (2009) Minimizing sparse higher order energy functions of discrete variables. In: *IEEE Conference on Computer Vision and Pattern Recognition*
- Schoenemann T, Cremers D (2008) High resolution motion layer decomposition using dual-space graph cuts. In: *IEEE Conference on Computer Vision and Pattern Recognition*
- Spangenberg R, Langner T, Rojas R (2013) Weighted semi-global matching and center-symmetric census transform for robust driver assistance. In: *Computer Analysis of Images and Patterns*
- Sun D, Sudderth EB, Black MJ (2010) Layered image motion with explicit occlusions, temporal consistency, and depth ordering. In: *Neural Information Processing Systems*
- Sun D, Wulff J, Sudderth E, Pfister H, Black M (2013) A fully-connected layered model of foreground and background flow. In: *IEEE Conference on Computer Vision and Pattern Recognition*
- Tao H, Sawhney HS (2000) Global matching criterion and color segmentation based stereo. In: *IEEE Workshop on Applications in Computer Vision*
- Unger M, Werlberger M, Pock T, Bischof H (2012) Joint motion estimation and segmentation of complex scenes with label costs and occlusion modeling. In: *IEEE Conference on Computer Vision and Pattern Recognition*
- Valgaerts L, Bruhn A, Zimmer H, Weickert J, Stoll C, Theobalt C (2010) Joint estimation of motion, structure and geometry from stereo sequences. In: *European Conference on Computer Vision*
- Vaudrey T, Rabe C, Klette R, Milburn J (2008) Differences between stereo and motion behaviour on synthetic and real-world stereo sequences. In: *International Conference on Image and Vision Computing New Zealand*
- Vedula S, Baker S, Collins R, Kanade T, Rander P (1999) Three-dimensional scene flow. In: *IEEE Conference on Computer Vision and Pattern Recognition*
- Veksler O, Boykov Y, Mehrani P (2010) Superpixels and supervoxels in an energy optimization framework. In: *European Conference on Computer Vision*
- Vogel C, Schindler K, Roth S (2011) 3D scene flow estimation with a rigid motion prior. In: *IEEE International Conference on Computer Vision*
- Vogel C, Roth S, Schindler K (2013a) An evaluation of data costs for optical flow. In: *Pattern Recognition (Proc. of GCPR)*, pp 343–353
- Vogel C, Schindler K, Roth S (2013b) Piecewise rigid scene flow. In: *IEEE International Conference on Computer Vision*
- Vogel C, Roth S, Schindler K (2014) View-consistent 3D scene flow estimation over multiple frames. In: *European Conference on Computer Vision*
- Volz S, Bruhn A, Valgaerts L, Zimmer H (2011) Modeling temporal coherence for optical flow. In: *IEEE International Conference on Computer Vision*
- Wang JYA, Adelson EH (1994) Representing moving images with layers. *IEEE Transactions on Image Processing* 3:625–638
- Wedel A, Rabe C, Vaudrey T, Brox T, Franke U, Cremers D (2008) Efficient dense scene flow from sparse or dense stereo data. In: *European Conference on Computer Vision*
- Werlberger M, Trobin W, Pock T, Wedel A, Cremers D, Bischof H (2009) Anisotropic Huber-L1 optical flow. In: *British Machine Vision Conference*
- Yamaguchi K, Hazan T, McAllester D, Urtasun R (2012) Continuous Markov random fields for robust stereo estimation. In: *European Conference on Computer Vision*

- Yamaguchi K, McAllester D, Urtasun R (2013) Robust monocular epipolar flow estimation. In: IEEE Conference on Computer Vision and Pattern Recognition
- Yamaguchi K, McAllester D, Urtasun R (2014) Efficient joint segmentation, occlusion labeling, stereo and flow estimation. In: European Conference on Computer Vision
- Zabih R, Woodfill J (1994) Non-parametric local transforms for computing visual correspondence. In: European Conference on Computer Vision

## A Higher-order Reductions for Occlusion Handling with a Reference View

We here describe how to convert the occlusion-sensitive data term from Eq. (17) into a quadratic pseudo-Boolean function. Note that the only interesting case is  $|\mathcal{O}_p^0| \geq 2$ , that is there are two or more possibly occluding pixels. Otherwise, the problem is already in quadratic form ( $|\mathcal{O}_p^0| = 1$ ), or there is no occluding pixel and only the (unary) data term is required ( $|\mathcal{O}_p^0| = 0$ ).

Recall that Eq. (17) is defined as part of a single  $\alpha$ -expansion step, *i.e.* a pixel can only be assigned two possible labels ( $\alpha$  or its previous label). For simplicity we restrict the analysis to the case  $i = 0$ . We thus consider the term

$$\hat{u}_p^0[x_p = 0] \prod_{(\mathbf{q}, j) \in \mathcal{O}_p^0} [x_q \neq j]. \quad (25)$$

The reduction for  $i = 1$  is analogous.

First, let us consider the special case in which there is a pixel  $\mathbf{q}$  that occludes pixel  $\mathbf{p}$  in both possible assignments of  $x_q$ , that is  $(\mathbf{q}, 0) \in \mathcal{O}_p^0$  and  $(\mathbf{q}, 1) \in \mathcal{O}_p^0$ . In that case the pixel  $\mathbf{p}$  is always occluded and Eq. (25) vanishes. For the remaining cases, we distinguish between  $\hat{u}_p^0 < 0$  and  $\hat{u}_p^0 > 0$ .

*Case  $\hat{u}_p^0 < 0$ :* We can substitute the whole term with the help of at most one non-submodular term with weight  $\hat{u}_p^0$ . No non-submodular term is introduced if all Boolean variables in the term are inverted, *i.e.*  $j \equiv 1$ . In that case Eq. (25) becomes

$$\hat{u}_p^0(1 - x_p) \prod_{(\mathbf{q}, 1) \in \mathcal{O}_p^0} (1 - x_q). \quad (26)$$

Introducing an additional variable  $z$ , the polynomial in Eq. (26) can be replaced by

$$\min_z \hat{u}_p^0 \left( 1 - z - (1 - z)x_p - \sum_{(\mathbf{q}, 1) \in \mathcal{O}_p^0} (1 - z)x_q \right) \quad (27)$$

in quadratic form.

If  $x_p = 0$  and the other variables encode a constellation where  $\mathbf{p}$  is not occluded, then the expression becomes equal to  $\hat{u}_p^0$  (by setting  $z = 0$ ). Otherwise, the minimum is attained at 0 (with  $z = 1$ ).

In the case of there being a  $(\mathbf{q}, 0) \in \mathcal{O}_p^0$ , we follow the scheme introduced by Rother et al (2009). With the introduction of two auxiliary variables  $z_0, z_1$ , we replace the product in Eq. (25) by

$$\min_{z_0, z_1} -\hat{u}_p^0(z_0 z_1 - z_1 + (1 - z_0)x_p) - \hat{u}_p^0 \sum_{(\mathbf{q}, j) \in \mathcal{O}_p^0} \left( z_1(1 - x_q) + (1 - z_0)x_q \right). \quad (28)$$

Here, the term  $-\hat{u}_p^0 z_0 z_1$  is not submodular. Like in the previous case, if the variables do not encode an occlusion, and if  $x_p = 0$ , the minimum is  $\hat{u}_p^0$  (setting  $z_0 = 0$  and  $z_1 = 1$ ). Otherwise the minimum is 0 (setting  $z_0 = 1$  and  $z_1 = 0$ ).

*Case  $\hat{u}_p^0 > 0$ :* We approach this problem using a series of substitutions. Following Ali et al (2008) we replace a product of two variables in Eq. (25),  $x_{q_1} x_{q_2}$ , with a new variable  $z$ , and add

$$\min_z \hat{u}_p^0 (x_{q_1} x_{q_2} - 2x_{q_1} z - 2x_{q_2} z + 3z), \quad (29)$$

such that after the substitution Eq. (25) becomes

$$\hat{u}_p^0 (x_{q_1} x_{q_2} - 2x_{q_1} z - 2x_{q_2} z + 3z) + \hat{u}_p^0 (1 - x_p) z \prod_{\substack{(\mathbf{q}, j) \in \mathcal{O}_p^0 \\ \{(\mathbf{q}_1, 0), (\mathbf{q}_2, 0)\}}} [x_q \neq j]. \quad (30)$$

Two inverted Boolean variables can be replaced in the same manner. Note that we are not restricted to replacing only variables from  $\mathcal{O}_p^0$ , but can also substitute  $1 - x_p$  itself.

The substitution introduces one non-submodular term with weight  $\hat{u}_p^0$ . To arrive at a quadratic polynomial one needs to replace all but two literals of the product as described, leading to  $n - 1$  or  $n - 2$  non-submodular terms.

# Multi-View Normal Field Integration for 3D Reconstruction of Mirroring Objects

Michael Weinmann, Aljosa Osep, Roland Ruiters, Reinhard Klein  
University of Bonn  
Friedrich-Ebert-Allee 144, 53113 Bonn

`mw@cs.uni-bonn.de`, `osep@cs.uni-bonn.de`, `ruiters@cs.uni-bonn.de`, `rk@cs.uni-bonn.de`

## Abstract

*In this paper, we present a novel, robust multi-view normal field integration technique for reconstructing the full 3D shape of mirroring objects. We employ a turntable-based setup with several cameras and displays. These are used to display illumination patterns which are reflected by the object surface. The pattern information observed in the cameras enables the calculation of individual volumetric normal fields for each combination of camera, display and turntable angle. As the pattern information might be blurred depending on the surface curvature or due to non-perfect mirroring surface characteristics, we locally adapt the decoding to the finest still resolvable pattern resolution. In complex real-world scenarios, the normal fields contain regions without observations due to occlusions and outliers due to interreflections and noise. Therefore, a robust reconstruction using only normal information is challenging. Via a non-parametric clustering of normal hypotheses derived for each point in the scene, we obtain both the most likely local surface normal and a local surface consistency estimate. This information is utilized in an iterative min-cut based variational approach to reconstruct the surface geometry.*

## 1. Introduction

3D reconstruction is one of the fundamental problems in computer vision. It has remained in the focus of research since decades with many applications in *e.g.* industry, entertainment and cultural heritage. While a huge amount of techniques has been developed in this field, today's challenges can be found when considering surfaces which exhibit a complex surface reflectance behavior. In this paper, we focus on reconstructing mirroring objects. For such objects, most traditional techniques such as laser scanners, structured light or multi-view stereo are not applicable.

Assuming a perfect mirroring surface, the appearance of

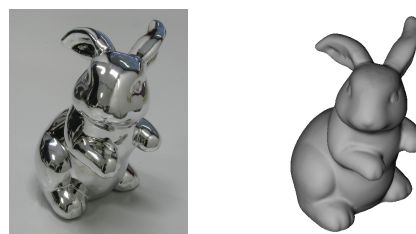


Figure 1: Bunny figurine and reconstructed model.

a surface point only depends on the surrounding environment, the viewing angle and the local surface normal. By controlling the environment, it is directly possible to estimate normal information [29, 9, 16]. An alternative is to rotate the object and to track the optical flow [1, 30].

Several approaches such as the ones in [9, 16] use these normals to perform a single-view normal field integration and are thus limited to partial 2.5D reconstructions. Others derive a normal consistency measure and perform a multi-view reconstruction (*e.g.* [6, 27]). However, normal consistency alone is not suitable to reconstruct fine surface details. Therefore, a final refinement step is performed in [27] to combine the geometry estimated from the normal consistency with the observed surface normals. However, none of the mentioned approaches has shown high-quality reconstructions for complex geometries in the presence of occlusions and interreflections.

To address this problem, we exploit the fact that outliers due to occlusions or interreflections are not consistent for different measurements taken under varying configurations of viewpoint and light source position. Inspired by the multi-view normal field integration approach presented in [8] but utilizing a numerical scheme for obtaining a globally consistent surface reconstruction similar to [35], we formulate the problem in terms of an optimization which combines both a local surface consistency measure

and the observed normal information. We determine these quantities in an outlier-robust way via mean-shift clustering [10] of the individual local normal hypotheses which result from different configurations of viewpoint and light position. This makes our approach capable of handling occlusions. To acquire the full shape of the considered object, the utilized setup comprises a turntable, eleven cameras and three screens for displaying structured light patterns which are reflected by the object surface. Our technique produces high-quality reconstructions of the full 3D shape of an object not only on synthetic but also on real-world data (see *e.g.* Figure 1).

In summary, the key contributions of our approach include a system for acquiring the full 3D shape of mirroring objects based on multi-view normal field integration and a novel clustering-based scheme for integrating different volumetric normal fields which is robust in the presence of outliers and noise and makes accurate 3D reconstruction possible on real-world data.

## 2. Related Work

Surface reconstruction has attracted a lot of research in the last decades. We focus on giving a brief review on normal-based reconstruction techniques and approaches for 3D reconstruction of highly specular and mirroring objects.

Amongst the early investigations for exploring normal information for 3D reconstruction are shape-from-shading techniques [20] and photometric stereo [36] which focused on reconstructing Lambertian objects from a single view under known light source positions. Since then, many techniques focused on extending photometric stereo towards general unknown illumination [4, 37] and providing robustness to violations of the underlying assumption of Lambertian reflectance behavior due to specularities or shadows. Other methods addressed a more general surface reflectance behavior such as spatially-varying BRDFs [18, 17]. However, effects such as shadows or interreflections are not taken into account. Furthermore, multi-view photometric stereo has been explored in *e.g.* [14, 5]. Targeting on the larger range of opaque materials, a reciprocal setup where camera and light source positions can be exchanged in order to exploit the Helmholtz reciprocity for calculating surface normals has been proposed in [42]. This principle has further been investigated in [13] in a multi-view setting.

Focusing on the reconstruction of specular objects, we refer to the surveys in [21, 3] and the theoretical discussion in [23]. Methods such as specular flow techniques [28, 1] compute the surface geometry from the movement of the environment features mirrored on the object surface. Such methods usually rely on a known motion of the mirroring object, its environment or the cameras respectively. However, estimating dense optical flow is non-trivial due to the possibility of observing a single environment feature sev-

eral times on the specular surface due to interreflections and usually a distant environment is assumed. For this reason, sparse reflectance correspondences have been used to locally approximate specular surfaces using quadrics in [30].

Other reconstruction approaches investigate the use of specular highlights observed on the object surface due to specular reflection in controlled environments. For this purpose, it is required to obtain dense observations of such specularities on the specular surface. This can be performed by moving the camera [43], using a moving light source [9], using extended light sources [22] or sequentially switching on individual elements of a grid of light sources [29]. As the number of required images increases linearly with the utilized light source positions, some techniques aim at significantly reducing the amount of required images by performing measurements in parallel. This can be achieved by rotating the object and using a circular light source [41] or by using printed, static or moving calibrated patterns [6, 31, 24]. Furthermore, some methods encode multiple light sources simultaneously. While encoding schemes for light source arrays have been investigated in [26], several approaches extend this idea by simulating a dense illumination arrays using LCD screens and encode the illumination emitted from the pixels using structured light patterns [16, 27, 38, 2]. However, in most of the approaches the assumption of far-field illumination or a distant environment is violated as the LCD display or the printed patterns have to be placed closely to the object for obtaining a sufficient sampling of light directions or feature directions.

The resulting normal-depth ambiguity can be solved in a multi-view setting such as the one presented in [6] where a calibrated pattern is used to produce reflections on the specular surface. Based on a volumetric representation, the law of reflection is used to hypothesize a normal at each voxel. Subsequently, the surface is assumed to pass through the voxels with the most consistent normal hypotheses following a normal disparity measure. The idea of hypothesizing surface normals has already been investigated in *e.g.* [11, 25] for extending classical single-view photometric stereo by selecting only hypotheses which agree with the underlying model assumptions. In [19], several normal hypotheses are generated for each pixel from different lighting directions. The solution space is then reduced according to an agreement concerning monotonicity, visibility, and isotropy properties. This makes the approach applicable for both diffuse and specular surfaces. Instead of a reduced solution space, the approach presented in [5] determines a maximal set of inliers per voxel on which regular photometric stereo is applied in a multi-view approach. While producing good reconstructions on synthetic data, the estimated surface consistency tends to being localized non-accurately for real-world data due to the lack of a per-voxel normalization. Further investigations on matching

hypothesized normal information in the context of specular surface reconstruction include the approaches proposed in [34, 2]. In [2], overlapping deflectometric measurements from multiple views are used to reconstruct large mirroring surfaces. However, self-occlusions represent problems for this approach and the configuration of the individual views has to be performed manually. Clustering normal observations per pixel in a single-view setting via the k-means algorithm has been used in [39] for reconstructing transparent objects. Similar to [6], specular consistency between a set of views in a triangulation-based scheme using a display with Gray codes for illumination has been investigated in [27]. After triangulation, normals are refined for the estimated depth values in a similar way to the iterative scheme proposed in [32].

Closely related to our approach are the multi-view normal field integration approaches proposed in [8] and [12] in the context of photometric stereo. These overcome the problem of obtaining only 2.5D reconstructions of partial surfaces in the single-view case. In [8], an initial visual hull reconstruction is followed by an iterative surface evolution based on level sets in a variational formulation. As no global optimization is performed, the surface evolution is sensitive to the initial visual hull. In contrast, the technique proposed in [12] is based on a Markov Random Field (MRF) energy function where the surface is computed via min-cut to find a global minimum. This is followed by a smoothing step similar to the one applied in [8]. A surface orientation constraint has been included in the energy functional which enforces the reconstructed geometry to agree with the observed surface normals. Both techniques employ additional silhouette information which is very difficult to determine for mirroring objects. In contrast, our method only incorporates normal information and brings the multi-view normal integration to the domain of reconstructing mirroring objects.

### 3. Problem Statement

Given a set of  $\kappa_c$  calibrated cameras  $\mathcal{C}_i$  with  $i = 1, \dots, \kappa_c$  which are positioned to observe a mirroring object from different viewpoints and a set of  $j = 1, \dots, \kappa_s$  screens, our goal is to reconstruct the object surface  $\delta V$  of a mirroring object with volume  $V$  by utilizing only normal information recovered for the individual views. Apart from a smoothness prior, we do not incorporate any prior knowledge about the object geometry such as the assumption of rather flat surfaces [9, 16] or an initial visual hull reconstruction [8]. Furthermore, our approach should consider the possibility of self-occlusions of the object geometry. Due to the complexity of real-world scenarios, we also have to design our reconstruction technique to be robust to noise. In addition, violations of the assumption regarding the underlying reflectance model need to be handled to some de-

gree as well as incomplete normal fields which occur when no normal information can be derived for certain parts of the object surface. For this reason, we formulate the surface reconstruction as a variational energy minimization problem similar to [8] according to

$$\min_V \left\{ -\lambda_1 \int_{\delta V} \langle c\mathbf{N}, \mathbf{n} \rangle dA + \lambda_2 \int_{\delta V} \alpha dA \right\}, \quad (1)$$

where  $\lambda_1$  and  $\lambda_2$  denote weighting coefficients,  $c$  represents a scalar field of surface consistency and the consistency-scaled vector field  $c\mathbf{N}$  contains information about both the local probability of surface presence and the local normal information for the points in the volume and  $\alpha$  represents a regularization parameter. The first term in the functional (1) is minimized for high consistency values and a surface which is perpendicular to the observed normals  $\mathbf{n}$ . The second part represents a regularization term which enforces a minimal surface area to avoid overfitting by increasing the cost for oscillating surfaces. Similar to [35], the global optimization of this functional can be mapped to the optimization of the continuous min-cut functional [40]

$$\min_{\lambda} \left\{ \int_{\Omega} (1 - \lambda)C_s + \lambda C_t + C |\nabla \lambda| dV \right\} \quad (2)$$

via specifying  $C = \lambda_2 \alpha$ ,  $C_s = \lambda_1 \max \{0, \text{div}(c\mathbf{N})\}$  and  $C_t = \lambda_1 \max \{0, -\text{div}(c\mathbf{N})\}$ . We choose this formulation as it provides efficiency concerning memory consumption and alleviates metrification errors.

After describing the utilized setup in the following Section, we describe the technique to acquire and integrate the normal information in Section 5.

### 4. Acquisition System and Calibration

For the acquisition, we use a turntable-based setup illustrated in Figure 2, where eleven cameras with a resolution of  $2,048 \times 2,048$  pixels are positioned on a vertical arc. The calibration of the cameras and the turntable axis is performed using a rotating three-dimensional calibration target with robustly detectable markers. Similar to *e.g.* [16, 27], we use a monitor-based shape-from-specularity approach to simulate a dense illumination area. Two static displays with resolutions of  $2,048 \times 1,152$  and  $2,560 \times 1,600$  pixels are placed close to the objects for displaying patterns. Gray code patterns and their inverses are used for the unique identification of the reflection of each screen pixel on the mirroring surface with a small number of acquired images. For illuminating the object surface as completely as possible, we place the object onto the display of an Asus TF300T-1E031A tablet with a resolution of  $1,280 \times 800$  pixels, which is on top of the turntable and also used for displaying patterns. Both the monitor displays and the tablet display need to be placed in a way that provides a good coverage

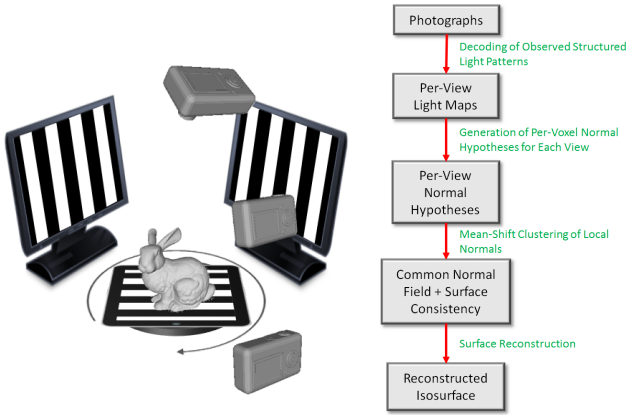


Figure 2: (left) Sketch of the utilized setup: The screens successively display the series of patterns for each rotation of the turntable. The reflected pattern on the object surface is observed by the cameras. For illustration purposes, only three of the eleven employed cameras are drawn. (right) Block diagram of the proposed method.

of the sphere of possible reflection directions. Additionally, we found it important that the tablet is stable enough to support the object weight in case of placing the object on it, *i.e.* tablets with hard glass surfaces are more suitable. In turn, this results in interreflections which have to be taken into account during the reconstruction.

For calibrating the positions of the utilized displays, we use the decoded pattern information observed in the images of the involved cameras and perform an estimation of the display pixel positions  $\mathbf{x}_l$  via triangulation so that the resulting point cloud represents (a part of) the display. From the decoded bits for each of the  $m$  points in the point cloud, it is possible to uniquely determine its offset  $\mathbf{u}_l = [u_l, v_l]^T$  from the origin  $\mathbf{o}$  of the display frame which we consider to be at the upper-left. Using this information, we can derive the coordinate frame of the screen consisting of the origin  $\mathbf{o}$  and the spanning vectors  $\mathbf{a}$  (parallel to the display width) and  $\mathbf{b}$  (parallel to the display height) via optimizing  $Q = \sum_{l=1}^m (\mathbf{x}_l - (\mathbf{o} + u_l \mathbf{a} + v_l \mathbf{b}))^2$ . The resulting linear system is solved using least squares minimization. Given the screen calibration, we can directly determine the 3D location of a pixel on the screen by considering its bit sequence.

For the calibration of the screens, it is not necessarily required to see the complete screens in the camera images as several parts of the displays seen in different cameras are sufficient. While our calibration method requires the monitor to be close to the object, this is eventually desirable for the measurement to cover a larger part of the mirror surface with the projected patterns and reduce the influence of light

fall-off.

## 5. Multi-View Shape-from-Coded-Illumination

For bringing classical shape-form-specularity techniques to the multi-view scenario, we first discuss the utilized encoding of the illumination patterns as well as the problems occurring due to surface curvatures which we solve via a fuzzy decoding of the patterns. Subsequently, we describe how the decoded information is used to generate normal hypotheses from which the normal field required in the optimization (1) and the surface consistency are derived. The block diagram of our method is shown in Figure 2.

### 5.1. Coded Illumination

For encoding the illuminations coming from the displays, we use Gray code patterns which enable a robust decoding. Additionally, similar to the approach presented in [33], we take the inverse patterns for increasing robustness. For decoding the displayed bit sequences, we compare the intensity values observed at each pixel  $\mathbf{u}$  in the pair consisting of image  $\mathcal{I}_{i,j,k,q}$  seen while displaying pattern  $\mathcal{P}_q$  and image  $\bar{\mathcal{I}}_{i,j,k,q}$  seen while displaying its inverse pattern  $\bar{\mathcal{P}}_q$ . If the difference is below a certain threshold, we mark the decoded bit as unreliable. We use  $|\mathcal{I}_{i,j,k,q} - \bar{\mathcal{I}}_{i,j,k,q}| < 0.1 \mathcal{I}_{i,j,k,0}$ , where  $\mathcal{I}_{i,j,k,0}$  represents the photo taken under illumination by the fully lit pattern.

As each pixel on the displays can be uniquely encoded and its 3D position on the screen is known from the screen calibration, observed codewords can directly be related to the corresponding 3D positions on the screen. Hence, we generate a light map [3, 9] for each individual camera under each rotation angle  $k$  of the turntable and under illumination from each display  $j$ . These light maps  $\mathcal{L}_{i,j,k}$  assign to each pixel in the camera image the light source position. In general, there will not be observations for all the pixels. The reason for this is that, depending on the shape of the object and the position of the illuminant, only a part of the surface will reflect patterns towards the camera.

Interreflections introduce outliers in the light maps. In addition, depending on the curvature of the mirroring surface and the differing relative distances to the display pixels or other effects, such as non-ideal or spatially varying reflectance properties, it is usually not possible to decode the complete bit sequence correctly. High-frequency patterns might appear blurred on the object surface which has already been observed in *e.g.* [16, 15, 3] and it is not possible to decide if pattern  $\mathcal{P}_q$  or its inverse  $\bar{\mathcal{P}}_q$  has been displayed. As a consequence, we introduce a fuzzy decoding. The basic idea is to only use the reliably decoded bits per pixel to identify the corresponding display area which illuminated this pixel. If less bits can be reliably decoded, the ambiguity in the region of the display which illuminated the pixel

increases. The corresponding light source position is determined as the center of this reliably decoded region.

To address noisy decodings in the light maps which could represent problems for the calculation of normals and, hence, also for the normal field integration algorithm, we additionally perform a subsequent filtering step. In this step, all decoded labels with less than  $t_{bits}$  reliably decoded bits for both horizontal and vertical stripe patterns are discarded. For calibrating the screens, we use  $t_{bits} = 9$  as a very accurate decoding is possible. During the reconstruction, we use  $t_{bits} = 5$ . Furthermore, we also consider for each image pixel per series of patterns the average of the individual contrasts observed for the individual patterns and their inverses to filter out unreliable decodings. In principle, the quality of the decodings can be used as weights for the quality of the normals derived from them. However, in the scope of this paper, we did not investigate this.

## 5.2. Generation of Normal Hypotheses

The light maps described in the previous subsection are used to derive information about surface normals. As our setup violates the assumption of distant illumination and the object surface is unknown a priori, the ambiguity concerning the depth of the surface along the view directions for the individual cameras cannot be discarded as in the case of far-field illumination. In our variational formulation, we therefore consider a volumetric representation to resolve this problem. In particular, the normal hypotheses are calculated separately for all the points along the view direction per pixel in each camera similar to [6] by utilizing the information stored in the light maps. For each point  $\mathbf{x}$  in the volume and each combination of camera index  $i = 1, \dots, \kappa_c$  screen index  $j = 1, \dots, \kappa_s$  and rotation index  $k = 1, \dots, \kappa_r$ , we compute a normal estimate  $\mathbf{n}_{i,j,k}(\mathbf{x})$ . Assuming that the object remains fixed and cameras and displays are rotated, we consider the coordinate  $\mathbf{x}$  relative to the turntable. Therefore, we obtain light directions  $\mathbf{l}_{j,k}(\mathbf{x})$  and view directions  $\mathbf{v}_{i,k}(\mathbf{x})$  which depend on the position in the volume  $\mathbf{x}$  and both on the rotation index  $k$  and the screen index  $j$  or camera index  $i$  respectively. Following the law of reflection, we obtain the normal estimate  $\mathbf{n}_{i,j,k}(\mathbf{x})$  as the bisector between  $\mathbf{l}_{j,k}(\mathbf{x})$  and  $\mathbf{v}_{i,k}(\mathbf{x})$ . At points close to the surface, normal hypotheses derived for different camera/screen/rotation configurations, for which the corresponding points are visible, have only a small variance and almost coincide with the true surface normal. In contrast, hypotheses contradict each other at points distant to the true surface.

However, as the cameras might directly observe certain parts of the displays as well, the light maps do not only contain information about the object to be reconstructed. For the reconstruction of the object geometry, these regions in the light maps should not be propagated into the volume in the process of generating normal hypotheses. For this

reason, our method also analyzes the 3D distance between the intersection of the view rays with the plane of the active display and the light source position stored in the light map. If this distance is small (we use a threshold of 3mm), it is a hint that the information stored in the light map belongs to the screen geometry and can be masked out.

## 5.3. Multi-View Normal Field Integration and Surface Consistency Estimation

The result of the normal calculation step is a set of normal fields assigned to the involved capture configurations  $(i, j, k)$ . These individual fields need to be combined to one common normal field which contains information about the best local normal and the surface consistency.

After combining the information in the volume of interest, we have several normal votes for the different points in this volume. For finding the true surface, we assume that, at a certain location  $\mathbf{x}$  on the object surface, the normal hypotheses from the different cameras agree with each other and with the true surface normal. In contrast, normal estimates from the different configurations  $(i, j, k)$  will contradict each other further away from the surface. However, due to effects such as outliers, noise, non-ideal calibration or the discretization of the volume, perfectly matching normals will hardly occur in real-world scenarios. Therefore, we can consider the observed normals as samples from an underlying probability distribution. Since the non-occluded normals should agree up to a small variance in the vicinity of the true surface, the underlying distribution should have a global maximum centered around the surface normal. Furthermore, its variance can be regarded as a measure for surface consistency. Similar measures have been used in [6, 27] for reconstructing highly specular and mirroring objects. As the information about visibility of points w.r.t. the involved cameras is unknown, we have to also take into account that several of the normals actually come from an occluded view in addition to the noise and outliers.

Modeling the probability density of normals under occlusions is challenging as it depends on the geometry of the considered object as well as on the placement of the involved cameras and screens. Therefore, we do not model the probability density function (pdf) via a parametric model but instead only make the simplifying assumption that the density is highest for the actual surface normal. This assumption is warranted as the actual surface normal is consistent over all views where the respective surface point has been observed, whereas the outliers should not be consistent over several views. Under this assumption, finding the normal direction corresponds to finding the largest mode of the pdf. For this reason, we decided to use mean-shift clustering [10] as a non-parametric technique as it neither requires assuming a model nor creates discretization artifacts. We

therefore define the pdf as

$$p_{\mathbf{x}}(\mathbf{n}) = \frac{1}{\kappa_c \kappa_s \kappa_r h^3} \sum_{i,j,k} K \left( \frac{\|\mathbf{n} - \mathbf{n}_{i,j,k}(\mathbf{x})\|}{h} \right), \quad (3)$$

and set the local normal estimate  $\mathbf{N}(\mathbf{x}) = \arg \max_{\mathbf{n}} p_{\mathbf{x}}(\mathbf{n})$  to the centroid of the highest mode of the pdf. Furthermore, we use the density at the centroid as a surface consistency measure which we denote with  $c(\mathbf{x}) = p_{\mathbf{x}}(\mathbf{N}(\mathbf{x}))$ .

In eq. (3),  $K$  represents the kernel function with bandwidth  $h$ . We experimented with both the Epanechnikov kernel and the Gaussian kernel and found the latter to result in a more accurate reconstruction. We heuristically determined  $h = 0.03$  which worked for all our datasets, but did not perform a complete evaluation on the sensitivity to this parameter. As an alternative, it is also possible to consider normal histograms. Then, the highest mode of the pdf corresponds to the bin with the maximum count. Though this would be faster, in our experiments, we did not reach the quality of the reconstructions when using mean-shift clustering.

#### 5.4. Surface Reconstruction

After calculating the estimates for the common volumetric normal field and the surface consistency as described before, we adapt the iterative optimization procedure presented in [35] to our setting. After an initialization of the utilized octree at a coarse level, the grid is successively refined according to the local surface consistency estimates in the volume. In a subsequent iterative process, the memory efficient continuous min-cut [40] is applied for a global optimization per iteration. In a final step, the resulting binary indicator function is smoothed inspired by the technique presented in [7].

### 6. Experimental Results

We evaluate our technique in two steps. To demonstrate the robustness of our reconstruction framework, we first consider the classical multi-view normal field integration case. Here, we use per-camera normal images as input. In the next step, we show results on mirroring objects. For the experiments mentioned in the paper, we use 264 views ( $\kappa_c = 11$  cameras are mounted on an arc and the turntable is rotated in steps of  $15^\circ$ , *i.e.*  $\kappa_r = \frac{360^\circ}{15^\circ} = 24$ ).

In a first experiment, we consider 3D reconstruction from several per-view normal fields. For this purpose, we have acquired a painted mask made of clay and estimate for each view an independent normal map using classical single-view photometric stereo [36]. Subsequently, the integration is performed using our variational formulation. We use the assumption of far-field illumination but with our technique it would also be possible to relax this assumption by computing an individual normal at each point in the volume. As the assumption of Lambertian surface reflectance



Figure 3: Results on a photometric stereo dataset: In particular, the painted regions of the clay mask exhibit specularities which leads to a violation of the assumption regarding Lambertian reflectance behaviour. Nevertheless, the reconstruction preserves the shape in these regions.

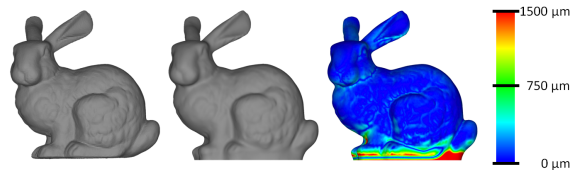


Figure 4: Stanford Bunny model, reconstructed model and visualization of the reconstruction error. Except for the bottom region, where almost no observations have been available, the reconstruction on an adaptive grid of level nine (at which the voxel edge length is approx.  $250\mu\text{m}$ ) fits to the original model.

is violated due to the presence of effects such as specular reflection, shadows and inter-reflections on the mask surface, normal estimation based on linear least-squares fitting is prone to errors. Therefore, we use a simple outlier rejection to remove the influence of too bright or too dark regions in the least-squares fitting. The reconstructed model is shown in Figure 3. Applying a more sophisticated photometric stereo technique would probably improve the reconstruction quality. We also show results for a synthetic test case in the supplementary material where normal fields are directly generated from the object geometry using a normal shader in OpenGL. The results demonstrate that fine surface details are well-preserved in the reconstruction.

For mirroring objects, we first consider a synthetic test case where we represent each display via a plane textured according to the patterns of the Gray code sequence. The scene is rendered using conventional ray tracing using 64 samples per pixel to accurately simulate the blurring in curved regions due to limited camera resolution. We use a camera resolution of  $2,048 \times 2,048$  pixels and simulate  $\kappa_s = 2$  screens which results in  $\kappa_s \cdot \kappa_c \cdot \kappa_r = 528$  light maps. Figure 4 shows a comparison of the original model and the reconstruction. For evaluating the robustness of our

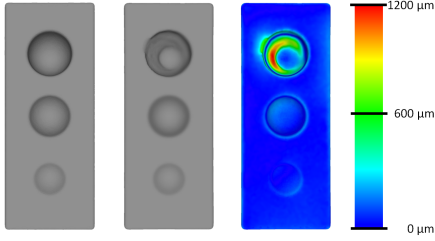


Figure 5: Block model with pits of increasing depth, reconstructed model and visualization of the reconstruction error (level nine reconstruction, *i.e.* the voxel edge length is approx.  $250\mu\text{m}$  at level nine).

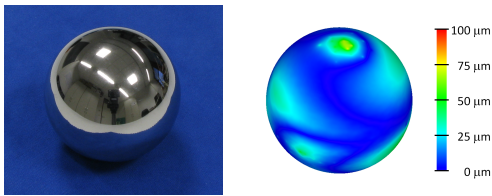


Figure 6: Reconstruction of a mirroring sphere (object and visualization of the Hausdorff distance between the reconstructed model and a sphere according to the sphere specifications).

approach w.r.t. interreflections, we also considered a synthetic, mirroring block with pits of increasing depth, where the proportion of multiple-bounce observations gradually increases. The reconstruction results are shown in Figure 5. Finally, we evaluate our technique on two mirroring, real-world objects. For obtaining information about the accuracy of our approach, we have measured a precisely manufactured sphere with a radius of 25 mm (using  $\kappa_s = 2$  screens) and compare the reconstructed model to an ideal sphere of fixed radius whose center is determined via a least squares fit. The error is measured via the Hausdorff distance and shown in Figure 6. The root mean square error of the reconstruction is  $20\mu\text{m}$  which is considerably lower than the edge length of a voxel (approx.  $200\mu\text{m}$ ) on the utilized maximum octree level. In comparison, one image pixel corresponds to approx.  $150\mu\text{m}$  at the distance of the object.

Furthermore, we test the robustness of our approach on objects with a more complex surface geometry such as self-occluded parts and concavities which lead to interreflections. For this purpose, we have acquired a mirroring bunny figurine. The reconstruction in Figure 1 clearly indicates the possible reconstruction accuracy. Using additional octree levels could further improve the reconstruction at the cost of higher computation effort and memory requirements.

During our experiments, we mainly start with an initial

subdivision on level seven and perform each times three surface adaptations before going to the next higher octree level. On a Intel Xeon E5654 CPU with 2.4 GHz, our level nine reconstruction for  $\kappa_r = 24$ ,  $\kappa_c = 11$  and  $\kappa_s = 3$ , as used for the real-world bunny figurine, requires approximately 12 hours, while the acquisition took approx. 2 hours.

The results shown in this section indicate the potential of normal-based surface reconstruction. In contrast to the previously presented multi-view normal field integration approaches in [8, 12], our method is robust enough to deal with real-world data in the presence of noise and outliers. However, regions such as concavities with a certain orientation to the displays, under which no information can be observed, cannot be accurately reconstructed.

## 7. Conclusions

In this paper, we have presented a novel, robust multi-view normal field integration technique for reconstructing the full 3D shape of mirroring objects. Based on coded illumination, our technique derives several normal hypotheses for each point of the considered volume. From these hypotheses, both the most likely local surface normal and a local surface consistency estimate are computed. In our experiments, we have demonstrated that our method yields accurate 3D reconstructions of highly-specular objects even in the presence of occlusions.

Current limitations can be found when considering deep concavities or other parts of the surface, where no information has been observed. Resolving these problems is challenging as it would require considering multiple scattering. Since the underlying optimization technique is independent of the source of the estimated normals, we would like to extend our method to objects which are only partially mirroring and also exhibit other surface reflectance behavior.

**Acknowledgements:** The research leading to these results was funded by the European Community’s Seventh Framework Programme (FP7/2007-2013) under grant agreement n° 323567 (Harvest4D); 2013-2016.

## References

- [1] Y. Adato, Y. Vasilyev, O. Ben-Shahar, and T. Zickler. Towards a theory of shape from specular flow. In *Proc. ICCV*, pages 1–8, 2007.
- [2] J. Balzer, S. Holer, and J. Beyerer. Multiview specular stereo reconstruction of large mirror surfaces. In *Proc. CVPR*, pages 2537–2544, 2011.
- [3] J. Balzer and S. Werling. Principles of Shape from Specular Reflection. *Measurement*, 43:1305–1317, 2010.
- [4] R. Basri, D. Jacobs, and I. Kemelmacher. Photometric stereo with general, unknown lighting. *IJCV*, 72:239–257.

- [5] M. Beljan, J. Ackermann, and M. Goesele. Consensus multi-view photometric stereo. In *DAGM/OAGM Symposium*, pages 287–296, 2012.
- [6] T. Bonfort and P. Sturm. Voxel carving for specular surfaces. In *ICCV*, pages 691–696, 2003.
- [7] F. Calakli and G. Taubin. Ssd: Smooth signed distance surface reconstruction. *Comput. Graph. Forum*, 30(7):1993–2002, 2011.
- [8] J. Y. Chang, K. M. Lee, and S. U. Lee. Multiview normal field integration using level set methods. In *CVPR*, pages 1–8, 2007.
- [9] T. Chen, M. Goesele, and H.-P. Seidel. Mesostructure from specularity. In *CVPR*, volume 2, pages 1825 – 1832, 2006.
- [10] Y. Cheng. Mean shift, mode seeking, and clustering. *TPAMI*, 17(8):790–799, 1995.
- [11] E. N. Coleman and R. Jain. Obtaining 3-dimensional shape of textured and specular surfaces using four-source photometry. *Computer Graphics and Image Processing*, 18(4):309 – 328, 1982.
- [12] Z. Dai. A markov random field approach for multi-view normal integration. Master-Thesis, University of Hong Kong, 2009.
- [13] A. Delaunoy, E. Prados, and P. N. Belhumeur. Towards full 3D Helmholtz stereovision algorithms. In *ACCV 2010 - Volume Part I*, pages 39–52, 2011.
- [14] C. H. Esteban, G. Vogiatzis, and R. Cipolla. Multiview photometric stereo. *TPAMI*, 30(3):548–554, 2008.
- [15] Y. Francken, T. Cuypers, T. Mertens, and P. Bekaert. Gloss and normal map acquisition of mesostructures using gray codes. *Advances in Vis. Computing*, pages 788–798, 2009.
- [16] Y. Francken, T. Cuypers, T. Mertens, J. Gielis, and P. Bekaert. High quality mesostructure acquisition using specularities. *CVPR*, pages 1–7, 2008.
- [17] D. B. Goldman, B. Curless, A. Hertzmann, and S. M. Seitz. Shape and spatially-varying brdfs from photometric stereo. In *ICCV*, volume 1, pages 341–348, 2005.
- [18] A. Hertzmann and S. M. Seitz. Example-based photometric stereo: Shape reconstruction with general, varying brdfs. *TPAMI*, 27(8):1254–1264, 2005.
- [19] T. Higo, Y. Matsushita, and K. Ikeuchi. Consensus photometric stereo. In *CVPR*, pages 1157–1164, 2010.
- [20] B. K. Horn. Shape from shading: A method for obtaining the shape of a smooth opaque object from one view. Technical report, Cambridge, MA, USA, 1970.
- [21] I. Ihrke, K. N. Kutulakos, H. P. A. Lensch, M. Magnor, and W. Heidrich. Transparent and specular object reconstruction. *Computer Graphics Forum*, 29(8):2400–2426, 2010.
- [22] K. Ikeuchi. Determining surface orientations of specular surfaces by using the photometric stereo method. *TPAMI*, 3(6):661–669, 1981.
- [23] K. N. Kutulakos and E. Steger. A theory of refractive and specular 3d shape by light-path triangulation. *IJCV*, 76(1):13–29, 2008.
- [24] M. Liu, K.-Y. K. Wong, Z. Dai, and Z. Chen. Specular surface recovery from reflections of a planar pattern undergoing an unknown pure translation. In *ACCV (2)*, pages 137–147, 2010.
- [25] A. Maki and R. Cipolla. Obtaining the shape of a moving object with a specular surface. In *Proc. BMVC*, pages 39.1–39.10, 2009.
- [26] S. Nayar, L. Weiss, D. Simon, and A. Sanderson. Specular Surface Inspection using Structured Highlight and Gaussian Images. *Transactions on Robotics and Automation*, 6(2):208–218, Apr 1990.
- [27] D. Nehab, T. Weyrich, and S. Rusinkiewicz. Dense 3D reconstruction from specularity consistency. In *CVPR*, 2008.
- [28] S. Roth and M. J. Black. Specular flow and the recovery of surface structure. In *Proc. CVPR*, volume 2, pages 1869–1876, 2006.
- [29] A. C. Sanderson, L. E. Weiss, and S. K. Nayar. Structured highlight inspection of specular surfaces. *TPAMI*, 10(1):44–55, 1988.
- [30] A. C. Sankaranarayanan, A. Veeraraghavan, O. Tuzel, and A. K. Agrawal. Specular surface reconstruction from sparse reflection correspondences. In *CVPR*, pages 1245–1252, 2010.
- [31] S. Savarese, M. Chen, and P. Perona. Local shape from mirror reflections. *IJCV*, 64(1):31–67, 2005.
- [32] M. Tarini, H. P. A. Lensch, M. Goesele, and H.-P. Seidel. 3d acquisition of mirroring objects using striped patterns. *Graph. Models*, 67(4):233–259, 2005.
- [33] M. Trobina. Error model of a coded-light range sensor. Technical report, Communication Technology Laboratory, ETH Zentrum, Zurich, 1995.
- [34] Z. Wang and S. Inokuchi. Determining shape of specular surfaces. In *Scandinavian Conference on Image Analysis*, pages 1187–1194, 1993.
- [35] M. Weinmann, R. Ruiters, A. Osep, C. Schwartz, and R. Klein. Fusing structured light consistency and helmholtz normals for 3d reconstruction. *BMVC*, Sept. 2012.
- [36] R. J. Woodham. Photometric method for determining surface orientation from multiple images. *Optical Engineering*, 19(1):139–144, 1980.
- [37] C. Wu, Y. Liu, Q. Dai, and B. Wilburn. Fusing multiview and photometric stereo for 3d reconstruction under uncalibrated illumination. *Transactions on Visualization and Computer Graphics*, 17(8):1082–1095, 2011.
- [38] M. Yamazaki, S. Iwata, and G. Xu. Dense 3d reconstruction of specular and transparent objects using stereo cameras and phase-shift method. In *ACCV (2)*, pages 570–579, 2007.
- [39] S. K. Yeung, T.-P. Wu, C.-K. Tang, T. F. Chan, and S. Osher. Adequate reconstruction of transparent objects on a shoestring budget. In *CVPR*, pages 2513–2520, 2011.
- [40] J. Yuan, E. Bae, and X.-C. Tai. A study on continuous max-flow and min-cut approaches. In *CVPR*, 2010.
- [41] J. Y. Zheng and A. Murata. Acquiring a complete 3d model from specular motion under the illumination of circular-shaped light sources. *TPAMI*, 22(8):913–920, 2000.
- [42] T. Zickler, P. N. Belhumeur, and D. J. Kriegman. Helmholtz stereopsis: Exploiting reciprocity for surface reconstruction. In *IJCV*, pages 869–884, 2002.
- [43] A. Zisserman, P. Giblin, and A. Blake. The information available to a moving observer from specularities. *Image and Vision Computing*, 7(1):38–42, 1989.